1

FUNDAMENTALS OF SURFACE ADHESION, FRICTION, AND LUBRICATION

Ali Faghihnejad and Hongbo Zeng

COPYRIGHTED MATERIAL

1.1 INTRODUCTION

The word *tribology* originates from the Greek word *tribos*, meaning rubbing. Tribology is the science of study of interacting surfaces in relative motion which encompasses interfacial phenomena such as friction, lubrication, adhesion, and wear. It spans a wide area of knowledge and technology from molecular and surface interactions to design of micro- and nano-mechanical systems. Although the term tribology has emerged only since 1966, the history behind it goes back to the prehistoric era, when man learned how to use force of friction for the generation of fire by rubbing two pieces of wood or flint stones against each other [1]. Later, the tribological achievements of early civilizations in developing wheeled vehicles, mills, rolling bearings, and the use of lubricants for transporting heavy stones were great advancements in the course of history. After the Industrial Revolution, the need for better machinery boosted the experimental and theoretical studies on different aspects of tribology such as bearing design, better lubricants, and so forth. The beginning of the twentieth century was accompanied by early investigations of friction and lubrication on the microscopic scale and development of theories on the molecular scale [1–3]. The development of modern tools such as surface forces apparatus (SFA) in the 1960s and 1970s, atomic force microscope (AFM) in the 1980s, and computers which allow molecular simulation of tribological

Polymer Adhesion, Friction, and Lubrication, First Edition. Edited by Hongbo Zeng.
© 2013 John Wiley & Sons, Inc. Published 2013 by John Wiley & Sons, Inc.

processes has greatly enhanced the research and knowledge in the broad field of tribology. One of the most exciting and rapidly growing areas of tribology research is biotribology, which covers a vast range of interests from live cell interfaces, artificial implants, and joint lubrication [4]. The importance of the research in tribology becomes more vital when it comes to economy, where more attention to friction and wear could save billions of dollars per year [5]. In this chapter, some basic concepts such as intermolecular and surface forces and surface energy are first discussed because of their fundamental importance in tribological processes. The basic principles of adhesion, friction, rolling friction, lubrication, and wear are discussed in Section 1.3. Section 1.4, Section 1.5, Section 1.6, and Section 1.7, respectively. The concept of real contact area is reviewed in Section 1.8 and some of the modern tools that are used extensively in tribological studies are discussed in Section 1.9. Finally, a brief review of the computer simulations in tribology is given in Section 1.10.

1.2 BASIC CONCEPTS

1.2.1 Intermolecular and Surface Forces

As tribology deals with two interacting surfaces in relative motion, the type of interaction that governs between the two surfaces is determinative of their tribological behavior. The intermolecular and surface forces can be attractive or repulsive and their range of action and magnitude can be very different. The types of forces operating between two surfaces depend on the nature of the interacting surfaces and medium between them. A comprehensive review of intermolecular and surface forces is beyond the scope of this chapter and only a brief overview is given here. The major types of nonspecific intermolecular and surface forces are listed in Table 1.1.

The *van der Waals* (VDW) forces exist between any two molecules or surfaces which can be attractive or repulsive, but always attractive between similar molecules. The VDW forces originate from interaction between electric dipole moments of the molecules. There are three major contributions to VDW forces: (1) a force between two permanent dipoles (Keesom interaction), (2) a force between a permanent dipole and a corresponding induced dipole (Debye interaction), and (3) a force between two instantly induced dipoles (London dispersion forces) [6]. The VDW interaction energy between two molecules or surfaces is given by

$$E(D) = -\frac{C_{VDW}}{D^6}, \tag{1.1}$$

and the corresponding force becomes:

$$F(D) = -\frac{dE}{dD} = -\frac{6C_{VDW}}{D^7}, \tag{1.2}$$

TABLE 1.1 Major Types of Nonspecific Intermolecular and Surface Interactions

Type of Interaction	Main Features
VDW	A force existing between all bodies. Usually attractive, and can be repulsive.
Electrostatic (coulomb, ionic, double layer)	A force existing between charged molecules/surfaces in liquid. Attractive or repulsive
Steric	A quantum mechanical force that is normally short range and increases very sharply as the two molecules get close (depending on geometry/shape or conformation of the interacting molecules)
Thermal fluctuation (i.e., osmotic, entropic, protrusion)	A temperature-dependent force associated with entropic confinement of molecular groups. Usually repulsive
Hydrophobic	An attractive interaction between hydrophobic molecules or surfaces in water. Usually long range
Solvation	Forces associated with local structuring of solvent molecules between interacting surfaces. For water, it is normally called hydration force.
Hydrogen bonding	A special electrostatic attractive interaction involving positively charged H atoms covalently bonded to electronegative atoms (e.g., N, O).

where D is the separation distance between the two molecules or surfaces, and C_{VDW} is a constant depending on the optical properties and geometry of the interacting bodies. The VDW interaction energy between two macroscopic bodies can be calculated assuming the interaction to be *additive*. Thus by integrating the interaction energy of all the molecules in one body with all the molecules in the other body, the two-body interaction energy would be obtained. The result of such analysis is summarized in Table 1.2 for different geometries in terms of Hamaker constant A,

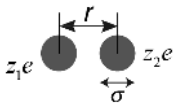
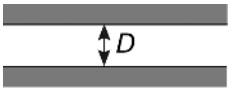
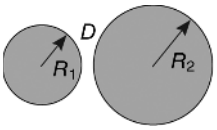
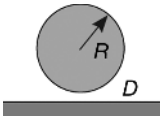
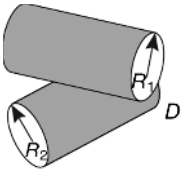
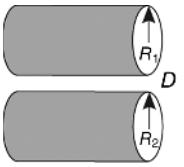
$$A = \pi^2 C_{VDW} \rho_1 \rho_2, \tag{1.3}$$

where ρ_1 and ρ_2 are the number density of the molecules in bodies 1 and 2, respectively. The Hamaker constant for two macroscopic bodies 1 and 2 interacting across a medium 3 is given by the Lifshitz theory as follows [7]:

$$\begin{aligned} A_{132} \approx{}& \frac{3}{4} k_B T \left(\frac{\varepsilon_1 - \varepsilon_3}{\varepsilon_1 + \varepsilon_3} \right) \left(\frac{\varepsilon_2 - \varepsilon_3}{\varepsilon_2 + \varepsilon_3} \right) \\ &+ \frac{3 h_P \nu_e}{8\sqrt{2}} \frac{\left(n_1^2 - n_3^2\right)\left(n_2^2 - n_3^2\right)}{\left(n_1^2 + n_3^2\right)^{1/2} \left(n_2^2 + n_3^2\right)^{1/2} \left\{ \left(n_1^2 + n_3^2\right)^{1/2} + \left(n_2^2 + n_3^2\right)^{1/2} \right\}}, \end{aligned} \tag{1.4}$$

where k_B is the Boltzmann constant (1.381×10^{-23} J/K), ε is the dielectric permittivity, n is the refractive index, h_P is the Planck's constant (6.626×10^{-34} m^2 kg/s), and ν_e is the main electronic absorption frequency.

TABLE 1.2 VDW and Electric Double-Layer Interaction Potential between Two Macroscopic Bodies of Different Geometries with Separation Distance D ($D \ll R$), and the Force Is Given by $F(D) = -dE(D)/dD$

Geometry of Two Bodies		$E_{vdw}(D)$	$E_{edl}(D)^a$
Two atoms or small molecules		$-C/r^6$	$\frac{z_1 z_2 e^2}{4\pi\varepsilon_0\varepsilon r}\frac{e^{-\kappa(r-\sigma)}}{1+\kappa\sigma}$
Two flat surfaces (per unit area)		$-A/12\pi D^2$	$(\kappa/2\pi)Ze^{-\kappa D}$
Two spheres		$-\left(\frac{R_1R_2}{R_1+R_2}\right)\frac{A}{6D}$	$\left(\frac{R_1R_2}{R_1+R_2}\right)Ze^{-\kappa D}$
Sphere-surface (per unit length)		$-AR/6D$	$RZe^{-\kappa D}$
Two crossed cylinders (per unit length)		$-A\sqrt{R_1R_2}\,/\,6D$	$\sqrt{R_1R_2}Ze^{-\kappa D}$
Two parallel cylinders (per unit length)		$-\sqrt{\frac{R_1R_2}{R_1+R_2}}\frac{A}{12\sqrt{2}D^{3/2}}$	$\sqrt{\frac{R_1R_2}{R_1+R_2}}\sqrt{\frac{\kappa}{2\pi}}Ze^{-\kappa D}$

[a]For similar constant potential surfaces of different geometries in symmetrical electrolyte solutions, such as NaCl and $MgSO_4$.

The *electrostatic double-layer* force is another major interaction that exists between two charged entities or surfaces in liquid solutions. When surfaces are charged in an electrolyte solution, the long-range, double-layer force comes to play a role. The electrostatic double-layer interaction energy between two similarly charged surfaces as a function of their separation is given by:

$$E(D) \approx +C_{DL}e^{-\kappa D}, \tag{1.5}$$

where C_{DL} is a constant that depends on geometry of the surfaces, solution conditions, and surface charge densities. The parameter $1/\kappa$ is the Debye length which depends only on electrolyte conditions (i.e., type and concentration) and temperature. The Debye length is the characteristic decay length of the

electrostatic double-layer interaction and decreases with increasing ionic strength of the solution, which is given as:

$$1/\kappa = \left(\varepsilon_0 \varepsilon_s k_B T \Big/ \sum_i \rho_{\infty i} e_0^2 z_i^2 \right)^{1/2}, \tag{1.6}$$

where ε_0 is the dielectric permittivity of free space, ε_s is the dielectric constant of solution, e_0 is the elementary charge of a single electron, $\rho_{\infty i}$ is the number density of ith ion in the bulk solution, and z_i is the valancy of the ith ion. The electric double-layer interaction energy for similar constant potential surfaces of different geometries in symmetrical electrolyte solutions (such as NaCl and $MgSO_4$) is given in Table 1.2 in terms of an interaction constant Z defined as [7]:

$$Z = 64\pi\varepsilon_0\varepsilon(k_B T/ze_0)^2 \tanh^2(ze_0\psi_0/4k_B T), \tag{1.7}$$

where Ψ_0 is the surface potential in millivolts and z is the electrolyte valency.

The sum of the VDW and double-layer forces between two surfaces form the so-called DLVO theory, after Derjaguin and Landau [8], and Verwey and Overbeek [9]. The VDW and double-layer forces depend differently on separation distance, the former being a power law while the latter an exponential law. VDW force is almost insensitive to solution conditions while double-layer force is significantly affected. As a result of these differences, DLVO forces can be repulsive or attractive depending on separation distance, solution conditions, and surface properties.

Steric and bridging forces normally occur between surfaces covered by large chain molecules (i.e., polymers, proteins) that can extend out into the solution. The net interaction between two polymer-covered surfaces includes the polymer–polymer and polymer–surface interactions, of which the former normally leads to steric forces while the latter leads to bridging forces. Polymer molecules can attach to a surface via either physical forces (physisorption) or chemical bonds (chemisorption). The state/conformation of an adsorbed polymer chain on a surface depends on parameters such as solution conditions, temperature, and type of adsorption. If a polymer is completely soluble in a solvent, then the polymer chain is expanded and conversely, in a poor solvent, the polymer chain tends to shrink. A polymer molecule is known as an ideal chain or freely connected chain if the monomers of the polymer chain are able to rotate freely about each other in any direction and their movement is not affected by the monomer–monomer interaction. In this state, the polymer molecule has a random coil conformation and its dimension is defined by the radius of gyration (R_g) as:

$$R_g = \frac{l\sqrt{N}}{\sqrt{6}}, \tag{1.8}$$

where l is the monomer length and N is number of monomer units in polymer chain. The solubility and state of a polymer in a solvent also depends on

temperature. The temperature in which a polymer molecule acts like a freely connected chain ($R = R_g$) is known as the theta temperature (T_θ) and a solvent at $T = T_\theta$ is known as theta solvent. The surface coverage Γ which is the number of adsorbed polymer chains per unit area is defined as:

$$\Gamma = \frac{1}{d^2}, \tag{1.9}$$

where d is the mean distance between the attachment points of adsorbed polymer chains. As two polymer-covered surfaces approach each other, a repulsive osmotic force is experienced between them, which is known as *steric* repulsion. The origin of this repulsive force is the unfavorable entropy associated with confining polymer chains between the two surfaces. When the surface coverage is low ($d > R_g$), also known as the mushroom regime, the repulsive steric interaction energy between two flat surfaces is given by [7]:

$$E(D) \approx 36\Gamma k_B T e^{-D/R_g}. \tag{1.10}$$

For high surface coverage ($d < R_g$) known as the *brush* regime, the repulsive steric force per unit area (pressure) between two flat surfaces is given by the Alexander–de Gennes equation as [7, 10]:

$$P(D) = \frac{k_B T}{d^3}\left[(2L/D)^{9/4} - (D/2L)^{3/4}\right] \quad \text{for } D < 2L, \tag{1.11}$$

where L is the thickness of the brush layer. The first term in Equation 1.11 is the osmotic repulsion and the second term is the elastic stretch energy of the chains. When two polymer-covered surfaces approach, the net interaction also depends on the forces between the polymer and the opposite surface that can be either repulsive or attractive. If the interaction between polymer and the opposite surface is attractive, then it is normally referred to as the bridging forces. In general, the bridging forces depend on the type of interaction (i.e., specific or nonspecific) between the polymer and the surface. Therefore, there is no single expression available for describing bridging forces, although linear or exponential dependence on distance have been observed in certain systems [7].

Hydrophobic force normally refers to the attractive force between two hydrophobic particles, surfaces, or molecules in water and aqueous solutions. Hydrophobic force has been reported to be much stronger than the theoretically expected VDW force. Experimental force measurements between various hydrophobic surfaces have intended to reveal the long-range nature of the force and corresponding strong adhesion force between the surfaces [11]. The magnitude of the hydrophobic force also depends on hydrophobicity of the surface, which is usually quantified by water contact angle measurement. The surfaces are normally considered to be hydrophobic if the water contact angle exceeds 90°. Nevertheless, the origin of the hydrophobic force is not fully

understood yet. Some of the suggested mechanisms include cavitation due to the metastability of a thin aqueous film separating the hydrophobic surfaces [12, 13], correlated dipole interactions [14], rearrangements of water molecules near hydrophobic surfaces [15], and the bridging of nanobubbles [16, 17].

Other intermolecular and intersurface interactions that are important in understanding the various tribological phenomena include, but are not limited to, thermal fluctuation forces, solvation forces, and hydrogen bonding. The reader is referred to other references for a more detailed discussion of the topic [7, 18].

1.2.2 Surface Energy

It is useful to introduce the concept of surface energy which will be used throughout the discussion. The energy required to separate unit areas of two surfaces 1 and 2 from contact is referred to as work of adhesion (W_{12}), and for identical surfaces it is called work of cohesion (W_{11}). The energy required to increase the surface area of medium 1 by unit area is surface energy or surface tension (γ_1), which is related to the work of cohesion by Equation 1.12:

$$W_{11} = 2\gamma_1. \tag{1.12}$$

For solids, the term surface energy is mostly used, which has the unit of energy per unit area (J/m^2), and for liquids, the term surface tension is usually used in units of force per unit length (N/m). The two terms are dimensionally and numerically the same although the term surface energy is more general in the sense that it can be applied to both liquids and solids. The surface tension of a liquid is the magnitude of the force exerted parallel to the liquid surface divided by the length of the line over which the force acts, which is determined by the cohesive forces between liquid molecules. The surface energy represents the excess energy that the molecules on the surface posses compared to molecules in the bulk of a material. There is a direct relationship between the surface energy and intermolecular forces of a material. The intermolecular forces that determine the boiling point and latent heat of a material also define its surface energy [7, 19]. Therefore, it is expected that materials with high boiling point usually have high surface energy (e.g., for mercury: $\gamma = 485$ mJ/m^2, $T_B = 357$°C) and lower boiling point substances have lower surface energy (e.g., for neon: $\gamma = 3.8$ mJ/m^2, $T_B = -246$°C). The surface energies and chemical structures of some common materials are given in Table 1.3. For surfaces between which attractive forces can be accounted for by conventional VDW forces, the surface energy can be approximated by Equation 1.13 [7]:

$$\gamma \approx \frac{A}{24\pi(r/2.5)^2}, \tag{1.13}$$

where r is the interatomic or intermolecular center-to-center distance (r/2.5~0.165 nm is commonly used) and A is the Hamaker constant. Equation

TABLE 1.3 Surface Energy and Chemical Structure of Some Common Materials

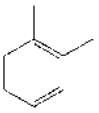
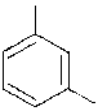
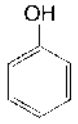
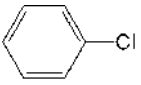
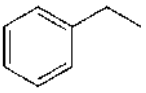
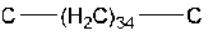
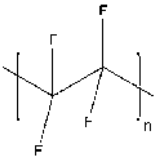
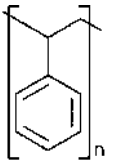
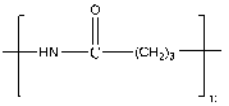
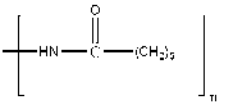
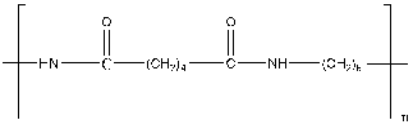
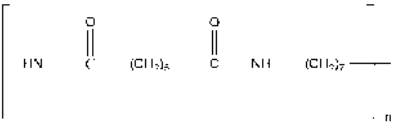
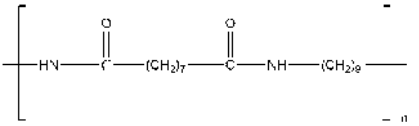
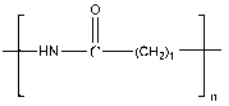
Material	Surface Energy γ (mJ/m^2)	Chemical Structure
Gold	1140	Au
Silver	903	Ag
Tungsten	2500	W
Aluminium	914	Al
Copper	1285	Cu
Mercury	486	Hg
Neon	3.8	Ne
Argon	9.4	Ar
Oxygen	10.7	O_2
Water	73.7	H_2O
Acetone	23.7	
Acetic acid	27.5	
Benzene	28.88 ± 0.03	
o-Xylene	30.10 ± 0.3	
m-Xylene	28.90 ± 0.1	
p-Xylene	28.37 ± 0.1	
Toluene	28.5 ± 0.3	
Phenol	40.9 ± 0.3	
Chlorobenzene	33.19 ± 0.1	
Ethylbenzene	29.20 ± 0.2	

TABLE 1.3 (*Continued*)

Material	Surface Energy γ (mJ/m^2)	Chemical Structure
Cyclohexane	25	
n-Hexatriacontane	21	
Polytetrafluoroethylene (PTFE)	19	
Polystyrene (PS)	43	
Nylon 4	48.5	
Nylon 6	38.4	
Nylon 6-6	43	
Nylon 7-7	43	
Nylon 9-9	36	
Nylon 12	35.8	

(*Continued*)

TABLE 1.3 (*Continued*)

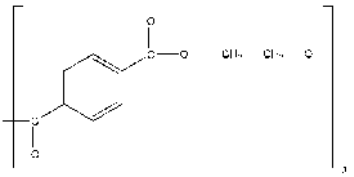
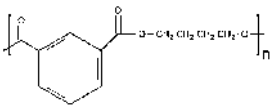
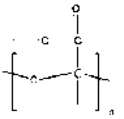
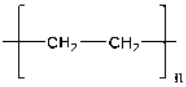
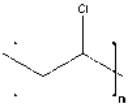
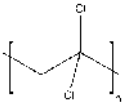
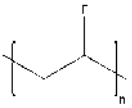
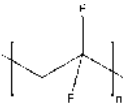
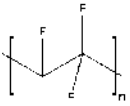
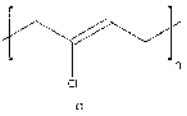
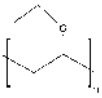
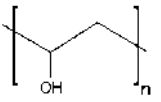
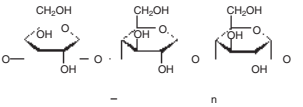
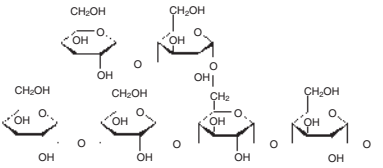
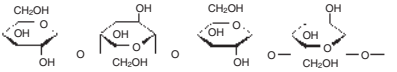
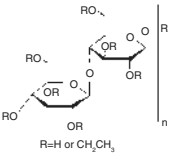
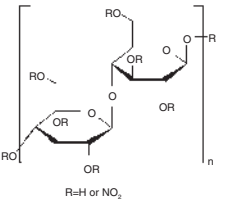
Material	Surface Energy γ (mJ/m^2)	Chemical Structure
Polyethylene terephthalate (PET)	43	
Poly(butylene isophthalate)	47.8	
Poly methy methacrylate (PMMA)	39	
Low density polyethylene (LDPE)	35	
Polyvinyl chloride (PVC)	42	
Polyvinylidene chloride (PVDC)	43	
Polyvinyl fluoride (PVF)	35	
Polyvinylidene fluoride (PVDF)	25	
Poly(trifluoroethylene)	22	
Poly(chloroprene)	43.6	
Poly(vinyl acetate)	36.5	

TABLE 1.3 (*Continued*)

Material	Surface Energy γ (mJ/m^2)	Chemical Structure
Poly(vinyl alcohol)	37	
Amylose	37	
Amylopectin	35	
Cellulose (from cotton)	42	
Ethyl cellulose	32	
Nitrocellulose	38	

Data compiled from different sources, including Knovel.com and Reference [7].

1.13 predicts the surface energy of nonpolar and nonmetallic compounds well. For metals, another attractive surface interaction (i.e., metallic bond) also exists, which is much stronger than conventional VDW forces and is due to electron exchange interactions at short separations. The metallic bonds are responsible for the much higher surface energy of metals compared to other materials (see Table 1.3). Moreover, the surface energy of metals and crystalline materials is very sensitive to the lattice mismatches. Since the atoms of two mismatched lattices cannot pack together as closely as that of two perfectly matched lattices, the adhesion energy of mismatched interface is usually significantly lower [7, 20]. Other contributions to the surface energy can be from charge exchange interactions such as acid–base and hydrogen bonding.

The surface and interfacial energies also determine the shape of a liquid droplet on a surface. One of the most widely used methods for measuring surface energy of a material is based on measuring the liquid droplet contact angel θ. If a droplet of liquid 2 forms a contact angle θ on a surface of material 1 in a medium 3, the interfacial energies are related by the well-known Young's equation as:

$$\gamma_{12} + \gamma_{23}\cos\theta = \gamma_{13}. \tag{1.14}$$

If medium 3 is air, Equation 1.14 can be simplified to:

$$\gamma_{12} + \gamma_2\cos\theta = \gamma_1. \tag{1.15}$$

Only γ_2 and θ can be directly measured by experiments, and thus there are two unknowns in Equation 1.15: γ_{12} and γ_1. Different approaches have been suggested to resolve this problem. Zisman et al. [21, 22] found that a plot of $\cos\theta$ versus γ_2 for a homologous series of liquids (so-called Zisman plot) usually generates a straight line and the intercept of such plot with the horizontal line $\cos\theta = 1$ is called the critical surface tension γ_c, which can be approximated as the solid surface energy γ_1. This approach should be used with caution as it is assumed that when $\cos\theta = 1$, γ_{12} is zero, which may not be necessarily true.

Another widely used method was developed by van Oss et al. [23] In the van Oss method, the surface energy is comprised of two terms which take into account the relative contributions from Lifshitz–VDW (γ^{LW}) and Lewis acid–base (γ^{AB}) interactions as:

$$\gamma = \gamma^{LW} + \gamma^{AB}. \tag{1.16}$$

The Lewis acid–base component of the surface energy is defined such that it comprises all the electron–acceptor and electron–donor interactions given by:

$$\gamma^{AB} = 2\sqrt{\gamma^+\gamma^-}. \tag{1.17}$$

Based on Equation 1.16 and Equation 1.17, the Young's equation can be written as:

$$\gamma_2(\cos\theta + 1) = 2\left(\sqrt{\gamma_1^{LW}\gamma_2^{LW}} + \sqrt{\gamma_1^+\gamma_2^-} + \sqrt{\gamma_1^-\gamma_2^+}\right). \tag{1.18}$$

Therefore, at least three different liquids should be used in contact angle measurements to obtain the three components of the surface tension of solid $\gamma_1^{LW}, \gamma_1^+, \gamma_1^-$ in Equation 1.18 and thus the total surface energy in Equation 1.16.

1.3 ADHESION AND CONTACT MECHANICS

Adhesion is the process of attraction between two particles or surfaces which brings them into contact. For the attracted particles or surfaces of the same material, this process is normally referred to as *cohesion*. Although at first sight

there might not be any direct relation between tribology and adhesion (while one deals with surfaces in *relative motion*, the other tends to bring them into *contact*), adhesion plays a crucial role in tribological phenomena, specifically friction and wear. Adhesion also plays an important role in a wide range of practical applications from adhesives, to cold welding of metals, to biomedical applications. Research on developing better adhesives in automotive and aerospace industries has continued for decades. Understanding the adhesion mechanisms of cells, bacteria, and proteins on biomedical surfaces is critical for the advances of biotechnology and biomedical science. In this section, the classical theoretical models for the adhesion or contact of two elastic surfaces are reviewed, which are commonly known as *contact mechanics* theories for analyzing surface deformations, stress distribution, and strength of the adhesion between two surfaces in contact.

1.3.1 Hertz Model

The deformation of two elastic surfaces in contact was first studied by Hertz in 1886 [24]. Hertz assumed that no adhesion was present between the two contacting surfaces, and analyzed the stress distribution and contact geometry of two spheres as a function of compressive load ($F_\perp$). Based on the Hertz theory, the radius a of contact area under compressive load $F_\perp$ is given by Equation 1.19 for two spheres of radii R_1 and R_2, Young's moduli E_1 and E_2, and Poisson ratio υ_1 and υ_2 , where R and K are given by Equation 1.20 and Equation 1.21:

$$a^3 = \frac{RF_\perp}{K}, \tag{1.19}$$

$$\frac{1}{R} = \frac{1}{R_1} + \frac{1}{R_2}, \tag{1.20}$$

$$\frac{1}{K} = \frac{3}{4}\left[\frac{1-\upsilon_1^2}{E_1} + \frac{1-\upsilon_2^2}{E_2}\right]. \tag{1.21}$$

And the pressure or normal stress distribution within the contact area is given by:

$$P(x) = \frac{3Ka\left(1-x^2\right)^{1/2}}{2\pi R}, \tag{1.22}$$

where $x = r/a$ (see Fig. 1.1). According to Equation 1.22, pressure at the center of contact region ($x = 0$) is $P(0) = (3F_\perp/2\pi a^2)$ that is 1.5 times of the mean pressure across the contact area. Hertz studied the contact of glass spheres by using an optical microscope and verified his theory experimentally. Based on the Hertz theory, there is infinite repulsion between the surfaces at $D = 0$; thus, during the unloading process, the surfaces separate when contact area decreases to zero as the compressive load reduces to zero (see Eq. 1.19).

1.3.2 Johnson–Kendall–Roberts Model

The main limitation of the Hertz theory is that it neglects the surface energy in the contact of two surfaces. For the first time, in 1921, Griffith pointed out the role of surface energy in elastic contact and fracture of solids [25]. He stated that during the formation of a crack in an elastic body, work must be done to overcome the attractive forces between the molecules of the two sides of the crack. He further pointed out that if the width of a crack is greater than the radius of the molecular action, the molecular attractions are negligible across the crack except near its end. Thus, Griffith stated that the conventional theory of elasticity is capable of analyzing the stresses correctly at all points of an elastic body except those near the end of a crack where molecular attractions cannot be neglected. For the same reason, there was a lot of controversy about the stress distribution and surface deformation at the edge of contact region until almost five decades after Griffith's paper (see Fig. 1.1) [26–32]. Although Griffith pointed out that surface forces deform the crack and affect the energy balance of the system, he did not quantify the model. The Hertz theory failed to predict the contact mechanics experiments performed by Johnson et al. using glass and rubber spheres: at low loads, the contact area was shown to be much bigger than that predicted by the Hertz theory and during the unloading process the contact radius reached a finite value before detachment [33]. Almost a century after the Hertz model, in 1971, Johnson, Kendall, and Roberts (JKR) proposed a model for contact of elastic surfaces

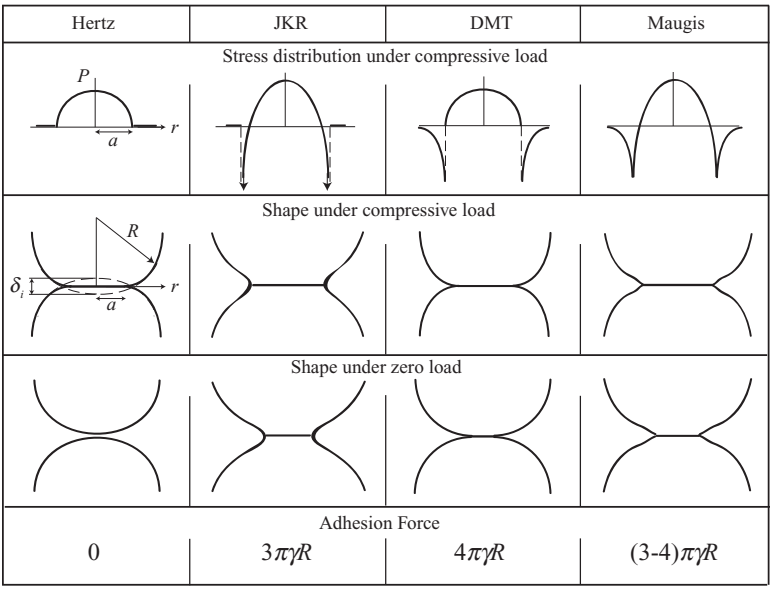


Figure 1.1 The main features of classical contact mechanics theories. (Modified based on Horn, R.G.; Israelachvili, J.N.; Pribac, F. (1987) Journal of Colloid and Interface Science, 115, 480–492.) © Elsevier.

which takes into account the role of surface forces [33]. They analyzed the contact between two elastic spheres and stated that equilibrium condition can be obtained when Equation 1.23 is satisfied:

$$\frac{dU_T}{da} = 0. \tag{1.23}$$

The total energy of the system (U_T) consists of three terms: the stored elastic energy, the mechanical energy under the applied load, and the surface energy. The appropriate expressions for these three components were derived and put into Equation 1.23 to obtain the relation shown in Equation 1.24, where W_{ad} is the adhesion energy and $W_{ad} = 2\gamma$ for two surfaces of the same materials:

$$a^3 = \frac{R}{K}\left(F_\perp + 3\pi R W_{ad} + \sqrt{6\pi R F_\perp W_{ad} + (3\pi R W_{ad})^2}\right). \tag{1.24}$$

When $W_{ad} = 0$ (non-adhesive), the Equation 1.24 (JKR theory) reduces to Equation 1.19 (Hertz theory). At zero load ($F_\perp = 0$), the contact area is finite and given by:

$$a^3 = \frac{6\pi R^2 W_{ad}}{K}. \tag{1.25}$$

The adhesion force (or so-called pull-off force) is the force required to separate the spheres from adhesive contact. The corresponding adhesion force between the spheres based on JKR theory is given by:

$$F_{JKR} = 3\pi R W_{ad} / 2. \tag{1.26}$$

And the normal stress distribution within the contact area is given by Equation 1.27, where $x = r/a$ (see Fig. 1.1):

$$P(x) = \frac{3Ka}{2\pi R}\left(1 - x^2\right)^{1/2} - \left(\frac{3KW_{ad}}{2\pi a}\right)^{1/2}\left(1 - x^2\right)^{-1/2}. \tag{1.27}$$

1.3.3 Derjaguin–Muller–Toporov Model

As shown in Equation 1.27, at the edge of contact region (i.e., $x = 1$), the normal stress is tensile and infinite in magnitude, which causes each surface to bend through a right angle along the contact edge. To resolve this unphysical situation, Derjaguin, Muller, and Toporov (DMT) [34] proposed another model for contact mechanics. According to DMT theory, adhesion arises from attractive surface forces but the surface shape outside the contact area is *assumed* to be Hertzian and not deformed by the surface forces. The stress distribution within the contact area is also assumed to be the same as that in Hertz theory. In the DMT model, the contact radius is given by Equation 1.28 and the adhesion (pull-off) force is given by Equation 1.29:

$$a^3 = \frac{R}{K}(F_\perp + 2\pi R W_{ad}), \tag{1.28}$$

$$F_{DMT} = 2\pi R W_{ad}. \tag{1.29}$$

1.3.4 Maugis Model

For a while there was some debate on which theory (JKR or DMT) is more suitable to explain the contact area dependence on the load [26–29]. Several models were proposed to show that either of the two theories (JKR and DMT) was a limiting case of a more general approach [30–32, 35, 36]. In these analyses, the intermolecular interaction between single asperities was described by a potential function. For examples, Muller et al. [31, 35] used a Lennard–Jones and Maugis [32] used a Dugdale potential function. In a unified model proposed by Maugis, the transition from JKR to DMT contact is determined by a dimensionless parameter, which is proportional to the parameter proposed by Tabor in 1977, generally known as the so-called Tabor number (Ta) shown in Equation 1.30 [26, 37],

$$Ta = \left(\frac{16 R W_{ad}^2}{9 K^2 z_0^3}\right)^{1/3}, \tag{1.30}$$

where z_0 is the equilibrium separation between the two surfaces in contact, and $W_{ad} = 2\gamma$ for the cohesion case. The Tabor number depends on the size of interacting particles, their elastic properties, and the characteristic length of molecular interaction of the materials. For soft materials with large surface energy and radius (i.e., $Ta >> 1$), JKR theory applies; while for hard materials with low surface energy and small radius (i.e., $Ta << 1$), DMT model would be more appropriate. The main features of contact mechanics theories are summarized in Figure 1.1.

1.3.5 Indentation

One of the most widely used methods for determining hardness and elastic modulus of materials is through indentation measurements. Basically an indenter is pushed against a sample surface through a complete cycle of loading and unloading, and the load–displacement profile is used to determine the hardness and elastic modulus. The indentation depth δ_i is the change in distance of the centers of the two approaching bodies from their (first contact and) undeformed state (see Fig. 1.1). The indentation experiments can be used to measure the mechanical properties of both bulk material and thin films or surface layers at the submicroscopic and nanoscales. For a cylindrical flat punch of radius a indenting an elastic material of Young's modulus E and Poisson's ration ν under applied load $F_\perp$, assuming no shear stress between the punch and the material surface, the indentation depth δ_i is given by Equation

1.31. Equation 1.31 shows that the indentation of a flat punch on an elastic plane is proportional to the applied load, which also assumes that the contact area πa^2 is constant and independent of the load during indentation:

$$\delta_i = \frac{1-\nu^2}{E}\frac{F_\perp}{a}. \tag{1.31}$$

The indentation depth δ_i of two elastic spheres in contact as given by different contact mechanics theories is given in Equation 1.32:

$$\text{Hertz: } \delta_i = \frac{a^2}{R} = \frac{F_\perp}{Ka}, \tag{1.32a}$$

$$\text{JKR: } \delta_i = \frac{a^2}{R} - \sqrt{\frac{16\pi\gamma a}{3K}}. \tag{1.32b}$$

In typical indentation experiments, a rigid punch is used such that deformation of the punch during the loading–unloading cycle is usually not significant. For simple punch geometries, Sneddon proposed that the relationship between load $F_\perp$ and elastic displacement δ_i can be generally written as [38, 39]:

$$F_\perp = c_1(\delta_i)^{c_2}, \tag{1.33}$$

where c_1 and c_2 are constants. The typical values of c_2 parameter are $c_2 = 1$ and 1.5 for cylindrical and spherical punches, respectively. One of the most widely used relationships for analyzing the indentation load-displacement data is given as [40]:

$$S = \frac{dF_\perp}{d\delta_i} = \frac{3}{2\sqrt{\pi}} K\sqrt{A_P}, \tag{1.34}$$

where $S = (dF_\perp/d\delta_i)$ is the slope of the unloading-displacement curve during initial stages of the unloading as measured experimentally, K is the combined modulus of indenter and specimen defined in Equation 1.21, and A_P is the projected area of elastic contact, which is usually assumed to be equal to the optically measured area of the hardness impression. The hardness of the sample material is given by:

$$H = \frac{F_{\perp,\max}}{A_P}, \tag{1.35}$$

where $F_{\perp,\max}$ is the maximum indentation load. As shown in Equation 1.34, reliable determination of elastic modulus depends on accurate measurement of unloading slope S and projected area A_p. For the measurement of unloading slope, S, Oliver and Pharr proposed a power law relationship to describe the unloading data as [40]:

$$F_\perp = c_3(\delta_i - c_4)^{c_5}, \tag{1.36}$$

where the parameters c_3, c_4, and c_5 can be determined by common fitting procedures. The unloading slope S can be calculated by differentiating Equation 1.36 and computing the derivative at the maximum load $F_{\perp,\max}$ and displacement $\delta_{i,max}$. The projected area A_p at maximum load $F_{\perp,\max}$ depends on the geometry of the indenter and the depth of contact. Oliver and Pharr assumed that the geometry of the indenter can be described by an area function $F_A(D)$, which relates the cross-sectional area of the indenter to the distance from the tip D. The projected contact area A_P at the maximum load can then be obtained as [40]:

$$A_P = F_A(\delta_{i,\max}). \tag{1.37}$$

The method of Oliver and Pharr has been widely used for the characterization of mechanical properties of different materials by indentation techniques, of which the latest refinements and advances have been reported in a recent review [41].

1.3.6 Effect of Environmental Conditions on Adhesion

All of the adhesion and contact models previously discussed assume contact between perfectly smooth surfaces. In reality, many factors can affect the contact of two surfaces, including contamination, load, surface roughness, and liquid films. Dust contamination can severely reduce the adhesion of metallic surfaces by preventing direct metallic contact [42, 43]. In an early study on gold surfaces, Williamson et al. found that if surface roughness is larger than the size of dust particles, then dust had little effect in preventing metallic contact. In contrast, if the dust particle protrudes the surface, it prevents intimate metallic contact and thus decreases the adhesion [42].

The presence of small amount of condensable vapors in the atmosphere is another parameter which can affect adhesion. The phenomenon of condensation of vapor molecules around the contact joints between the surfaces is known as *capillary condensation* and can have substantial effect on adhesive properties of surfaces. The condensed vapor forms a liquid meniscus between the two surfaces. As a result of the surface tension of liquid and curvature effect, a pressure difference occurs between the inside and outside of the meniscus known as Laplace pressure. The Laplace pressure of the meniscus pulls the two surfaces together and contributes to the adhesion force. The resulting adhesion force between a sphere of radius R on a flat surface in the presence of the liquid meniscus is given by:

$$F_{\text{adhesion}} = 4\pi R(\gamma_L \cos\theta + \gamma_{SL}) = 4\pi R\gamma_{SV}, \tag{1.38}$$

where θ is the contact angle of liquid on solid surface, γ_L is the surface energy of the liquid, and γ_{SL} and γ_{SV} are interfacial tensions of solid–liquid and solid–vapor interfaces, respectively. Usually $\gamma_L\cos\theta$ exceeds γ_{SL} and Equation 1.38 reduces to [7]:

$$F_{\text{adhesion}} = 4\pi R\gamma_L \cos\theta. \tag{1.39}$$

Thus adhesion force in the presence of the liquid meniscus is mainly determined by the surface energy of the liquid. Adhesion experiments that were done in an atmosphere of different vapors corroborate Equation 1.39 [44]. Recent experiments on the effects of relative humidity on adhesion have shown that adhesion regimes changes with humidity. Below a threshold relative humidity, adhesion is mainly determined by VDW forces and above that by capillary condensation [45, 46]. However, it should be noted that when the condensation continues and the Kelvin radius exceeds the sphere radius R (i.e., the particle becomes effectively immersed in excess liquid), the adhesion often turns to be very low due to the disappearance of the capillary term in Equation 1.38.

1.3.7 Adhesion of Rough Surfaces

Surface roughness is another critical parameter on adhesion. Generally, adhesion is conversely related to roughness for elastic surfaces [47–51]. The probability of intimate contact between two surfaces decrease with surface roughness, which therefore decreases the adhesion. Greenwood and Williamson [52] modeled a rough surface on which the asperities are assumed to have the same radius β and a Gaussian distribution of asperity heights z with mean height ω and standard deviation σ, as shown in Equation 1.40. It was assumed that the contact of each asperity follows the Hertzian model:

$$f(z) = \frac{1}{\sqrt{2\pi\sigma^2}} e^{-(z-\omega)^2/2\sigma^2}. \tag{1.40}$$

In 1975, Fuller and Tabor analyzed the adhesion between elastic solids and the effect of roughness. The asperities on the rough surfaces were assumed to follow the Gaussian distribution (similar to the Greenwood–Williamson model) and the contact of each asperity followed the JKR model [48]. Fuller and Tabor showed that the adhesion decreases with the "adhesion parameter" ($1/\Delta_c$), defined as:

$$\frac{1}{\Delta_c} = 3\sigma\left(\frac{2K}{9\pi\beta^{1/2}\Delta\gamma}\right)^{2/3}, \tag{1.41}$$

where $\Delta\gamma = \gamma_1 + \gamma_2 - \gamma_{12}$. Fuller and Tabor's model is valid only when the real contact area is much lower than the apparent contact area (see Section 1.7) and that contact breaks uniformly across the apparent contact area, but in real situations separation of surfaces from contact could be accompanied by crack propagation [53]. Other researchers applied different approaches such as using single-parameter characterization [48], double-parameter characterization [54], and fractals [55, 56] to model the surface roughness and the corresponding adhesion force. Nevertheless, there is no general mathematical model for

defining the surface roughness. Recent experimental measurement and theoretical modeling on adhesion of rough surfaces [56–59] showed an exponential relation between load $F_\perp$ and intersurface separation u as Equation 1.42, where u_0 is a constant:

$$F_\perp \propto e^{-u/u_0}. \tag{1.42}$$

According to recent experiments and theoretical modelings, the adhesion force decays exponentially with RMS surface roughness ς as [7]:

$$F_{ad}(\varsigma) = F_{JKR} e^{-\varsigma/\varsigma_0}, \tag{1.43}$$

where ς_0 is a constant and F_{JKR} is the JKR adhesion force for smooth surfaces ($\varsigma = 0$).

1.3.8 Adhesion Hysteresis

Another important aspect of adhesion process is hysteresis effects. Adhesion hysteresis is the difference between contact properties (e.g., contact area) during loading and unloading cycles. Adhesion hysteresis is usually defined as [60]:

$$\Delta\gamma = (\gamma_R - \gamma_A) \geq 0, \tag{1.44}$$

where γ_A is the advancing surface energy during loading and γ_R is the receding surface energy on unloading. $\Delta\gamma$ is a measure of energy dissipation during a complete loading–unloading cycle. Thus the adhesion energy hysteresis per unit area is given by:

$$W_{\text{hysteresis}} = 2(\gamma_R - \gamma_A) = 2\Delta\gamma. \tag{1.45}$$

For purely elastic material with no adhesion hysteresis, contact radius versus load curve would be essentially reversible for loading and unloading processes (see for example Eq. 1.24). However, for viscoelastic materials, the loading and unloading (contact radius vs. load) curves deviate as a result of hysteresis. The origin of hysteresis effects can be the inherent instabilities and irreversibilities associated with loading–unloading cycles or molecular rearrangements and interdigitations at the interface [61]. Recent experiments on polymer surfaces have revealed that polymers of lower molecular weight (MW) show higher adhesion and adhesion hysteresis due to the higher degrees of dynamic molecular rearrangements and interdigitation at the interface [62–64].

1.4 FRICTION

1.4.1 Amontons' Laws of Friction

The early investigations in the broad field of tribology were more focused on friction. One of the first scientific studies on tribology was performed by

Leonardo da Vinci (1452–1519), whose friction experiments resulted in statements that are mostly known as the Amontons' laws of friction, namely:

i. The friction force is directly proportional to the applied load.
ii. The friction force is independent of the apparent contact area.

The first law of Amontons is usually written mathematically as:

$$\mu = \frac{F_{\parallel}}{F_{\perp}}, \tag{1.46}$$

where $F_{\parallel}$ is friction force, $F_{\perp}$ is the normal load that presses the surfaces together, and μ is the coefficient of friction. In order to make the results of different experiments comparable to each other, it is a common practice to report the results of friction experiments in terms of coefficient of friction rather than friction force itself. Euler was the first one who distinguished between two modes of friction: static friction and dynamic friction [53]. The force needed to initiate relative movement of two bodies initially at rest is referred to as *static friction* force. When two bodies are in motion against each other, the force that resists the movement is referred to as dynamic or *kinetic friction*. Generally, the kinetic friction is lower than the static friction, but the values may depend on the actual experimental conditions [47]. The values of coefficient of friction for some common materials and systems are given in Table 1.4.

The role of surface texture in friction and the concept of asperity interaction were first introduced by Amontons in 1699 [1]. Later, in 1785, Coulomb investigated the role of surface area, nature of materials in contact, normal load, and contact time upon friction, mostly for wooden surfaces. Coulomb also studied the relationship between static and kinetic friction, and the third law of friction is often attributed to him which states:

iii. Kinetic friction is independent of the sliding velocity.

Amontons' laws of friction were originally concluded mostly based on experiments on wooden surfaces, which were later found to be valid for many other surfaces. However, it should be noted that Amontons' laws of friction are empirical laws, and exception to Amontons' laws have been observed in many systems and in various nanometric scenarios, as discussed further in this chapter.

1.4.2 The Basic Models of Friction

In spite of about 500 years of scientific study on friction, a theory has not yet been developed which can describe all experimental data available and predict friction between any two surfaces. A wide range of materials already have been tested in friction experiments such as wood [1, 65, 66], metals [67–69],

TABLE 1.4 Typical Values of the Coefficient of Friction for Material 1 Sliding on Material 2 at Different Environmental Conditions [7, 47]

Material 1	Material 2	Environment	Static μ_s	Kinetic μ_k
Gold	Silicon	Vacuum (10^{-8} Pa)	1.0	–
Gold	Gold	Air	2.8	–
Steel	Steel	Air, 20°C	0.58	–
Steel	Steel	Glycerine, 20°C	0.2	–
Steel	Steel	Olive oil, 20°C	0.11	–
Tungsten	Tungsten	Vacuum(10^{-8} Pa)	–	3.0
Tungsten	Tungsten	Vacuum(10^{-8} Pa), exposure to O_2	–	1.3
Ice	Ice	0°C	0.1	0.02
Ice	Ice	–70°C	0.5	0.09
Glass, tempered	PTFE	Air	0.10	0.10
Glass	Glass	Air	0.95	–
Silver	Alumina	Air	–	0.37
Diamond	Diamond	Air	0.1	–
Sapphire	Sapphire	Air	0.2	–
Mica	Mica	Air	1.0	–
Graphite	Graphite	Air	0.1	–
PMMA	PMMA	Air	0.80	–
PTFE	PTFE	Air	0.08	0.07
Nylon 6/6	Nylon 6/6	Air	0.06	0.07
Polystyrene	Polystyrene	Air	0.50	–
Polyethylene	Polyethylene	Air	0.20	–
440C steel	HDPE	Air	–	0.09
440C steel	LDPE	Air	–	0.40
440C steel	PP	Air	–	0.21
440C steel	PVDF	Air	–	0.31
Mild steel	Nylon 6/6	Air	0.20	0.28
Mild steel	Nylon 6/12	Air	0.24	0.31
Mild steel	Polystyrene	Air	0.28	0.32

crystalline solids [70–72], graphite [73–76], diamond [72, 73, 75, 77], mica [78–80], polymers [62–64, 81–83], and many more [49, 84–87]. A valuable list of available resources about friction can be referred to a recent review paper by Krim [88]. As pointed out by Dowson [1], there have been four major models or approaches in the long history of friction study, as follows:

i. *The geometrical or mechanistic model.* The geometrical or mechanistic model dominated most of friction studies until the beginning of the twentieth century. In this approach, asperity interaction and forces needed for asperities to slip over each other are believed to be the origin of the friction force. The work of early investigators, including Amontons

and Coulomb, who believed in the mechanical view of friction, is extensively reviewed by Dowson [1]. Briefly, it was believed that mechanical interlocking of asperities resists the motion of two bodies against each other and the work of frictional force is equal to the work done against the normal load in separating the asperities and sliding them over each other. Therefore, the effect of lubrication in reducing friction was explained by the assumption that lubricants fill the irregularities and gaps between these asperities. However, the geometrical or mechanistic approach could not explain a variety of experimental observations. For example, friction between two highly polished smooth metallic surfaces is higher than unpolished surfaces as a result of cold welding of asperities. If the interlocking of asperities was the origin of friction, one should expect the unpolished surface to have higher friction. Another example is that adsorbed films and monolayers on different surfaces can greatly change the friction while essentially maintaining the same surface roughness.

ii. *The molecular or adhesive model.* Ewing [47] and Hardy [2] were among the first to propose that the origin of friction is the surface forces and molecular adhesion at the interface. According to Hardy, lubricants reduce the molecular field of force between the solid surfaces, which in turn reduces the friction. Prandtl [1] and Tomlinson [89] considered the role of adhesion in the friction process and tried to analyze the friction at the molecular level. According to Tomlinson, when two surfaces are moved against each other, molecules are forced into each other's atomic fields and then separated, which is accompanied by energy dissipation that was considered to be the origin of the friction force. Derjaguin took into account the role of intermolecular forces, quantified the concept proposed by Tomlinson, and derived the following relation for friction force [3]:

$$\mu = \frac{F_{\|}}{A_{\text{real}}(P + P_0)}, \tag{1.47}$$

where A_{real} is the real contact area and P and P_0 are the mean stresses representing external forces (external load) and molecular adhesion, respectively.

iii. *The deformation or ploughing model.* In the deformation or ploughing model, friction is attributed to the force required to move hard asperities through or over another surface. Let A_0 be the sum of the area of indenting asperities perpendicular to the direction of sliding and H' be the mean stress required to shear the junction; the friction force would be given by:

$$F_{\|} = A_0 H'. \tag{1.48}$$

Let H be the yield stress of the softer material and note that normal load is applied on real contact area, one would have:

$$F_{\perp} = A_{\text{real}} H. \tag{1.49}$$

Therefore, the coefficient of friction becomes:

$$\mu = \frac{F_{\parallel}}{F_{\perp}} = \frac{A_0 H'}{A_{\text{real}} H} = \frac{A_0}{A_{\text{real}}}. \tag{1.50}$$

In Equation 1.50, it is assumed that H is equal to H', which is a realistic assumption in most cases [47]. In order to quantify the A_0/A_{real} ratio, the geometry of the asperities must be known. For example, for conical asperities that make an angle θ to the direction of sliding, the coefficient of friction is [1]:

$$\mu = \frac{A_0}{A_{\text{real}}} = \frac{2}{\pi} \tan\theta. \tag{1.51}$$

Similar expressions have been also derived for other geometries [1, 47].

iv. *Combined adhesive and ploughing model*. In the fourth approach (combined adhesive and ploughing model), it is believed that both adhesion and ploughing contribute to the friction force. Friction experiments on different metals [67, 69, 90] have shown that deformation and wear occur not only on the surface but to a great depth beneath the surface of the material. Thus friction is not simply a surface phenomenon that can affect the molecules on the surface but also can lead to deformations far beneath the surface molecular layer of the material. Therefore, in order to explain the observed phenomena, it was proposed that friction is due to both adhesion and ploughing. Thus, the proposed mechanism for the metallic friction is as follows: when two surfaces are put into contact, adhesion and cold welding occur at the points of real contact and during sliding; force is required to shear these metallic junctions and also to plough out the metal [47]. Thus friction force can be expressed as:

$$F_{\parallel} = F_{\text{ploughing}} + F_{\text{shearing}}. \tag{1.52}$$

The ploughing term is given by Equation 1.48 and the shearing term can be written as:

$$F_{\text{shearing}} = A_{\text{real}} s, \tag{1.53}$$

where s is the tangential stress required to shear the junctions. Thus coefficient of friction becomes:

$$\mu = \frac{A_{\text{real}} s + A_0 H'}{A_{\text{real}} H} = \frac{s}{H} + \frac{A_0}{A_{\text{real}}}. \tag{1.54}$$

Replacing the corresponding value of A_0/A_{real} from Equation 1.51, the coefficient of friction for conical asperities may be expressed as:

$$\mu = \frac{s}{H} + \frac{2}{\pi}\tan\theta. \tag{1.55}$$

Experiments on metals [47] have shown that the shearing usually occurs within the softer material, therefore the coefficient of friction is mostly determined by the physical properties (s and H) of the softer one of two sliding materials. Experimental [67, 91, 92] and theoretical [93–96] research has been done to investigate the relative contribution of either adhesion or ploughing to the total friction force. Generally, the ploughing term is more dependent on the geometry of the slider and the depth of the indentation in comparison with the adhesion term [47, 94, 96]. Nevertheless, the role of adhesion seems to dominate the ploughing in friction between metals, although it is difficult to be generalized categorically [1].

The total friction force (Eq. 1.52) can be also written as:

$$F_{\parallel} = \mu F_{\perp} + sA. \tag{1.56}$$

The first term in Equation 1.56 is referred to as the load-controlled contribution which mainly depends on the structure and topography of the surfaces, while the second term is known as the adhesion-controlled contribution which depends on both the topography and the intermolecular forces between the surfaces [7]. Equation 1.56 also shows that for adhesion-controlled friction (i.e., at low loads), the friction force is not directly proportional to normal load as predicted by Amontons' first law.

The relationship between adhesion and friction has also been studied by using the SFA technique [97–99]. It was found that friction is directly proportional to the adhesion hysteresis rather than adhesion itself. The relation between adhesion hysteresis and friction is schematically shown in Figure 1.2. The friction between two surfaces, as they move relatively by an elemental distance δ, can be divided into a full adhesion cycle: separating the surfaces, moving by distance δ, and then bringing them down to contact. The adhesion energy hysteresis per unit area during this adhesion cycle is given by Equation 1.45. However, it should be noted that during the friction cycle molecules of the two surfaces may not fully debond as they do during the adhesion cycle. Thus, energy loss during friction would be a fraction of the adhesion energy hysteresis or $2\Omega\Delta\gamma$, where Ω lies between 0 and 1. Equating the frictional work done when two surfaces of contact area A move relatively by a distance δ to the energy loss due to adhesion energy hysteresis, one would obtain the following relation [7]:

$$F_{\parallel}\delta = 2\Omega A\Delta\gamma. \tag{1.57}$$

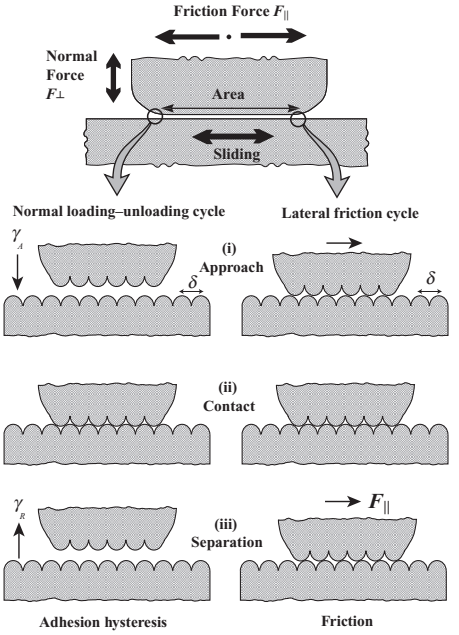


Figure 1.2 Relationship between adhesion hysteresis and "adhesion-controlled" friction.

Finally, the adhesion-controlled friction force would be:

$$F_{\|} = \frac{2\Omega A \Delta\gamma}{\delta}. \tag{1.58}$$

1.4.3 Stick-Slip Friction

One of the interesting phenomena in the process of friction that has been studied for a long time is the so-called *stick-slip* or *intermittent* motion. Instead of moving steadily, the two surfaces stick together and then slip past each other, which results in a sawtooth-like pattern in the friction trace (force vs. time). A typical experimental setup for tribological studies and friction trace with stick-slip motion is shown in Figure 1.3.

By definition, the maxima and minima of the stick-slip friction trace is referred to as static (F_s) and kinetic (F_k) friction. There are two main kinds of mechanisms for the stick-slip friction which depend on the type of friction: (1) dry friction and (2) lubricated friction. It should be noted here that there is still no single model available that can describe all the available experimental data on stick-slip friction behaviors. Each proposed model of stick-slip friction may not be generalized to other systems.

Let's first review the proposed mechanisms for stick-slip sliding during dry friction. Bowden and Tabor suggested that the stick-slip motion is due to the

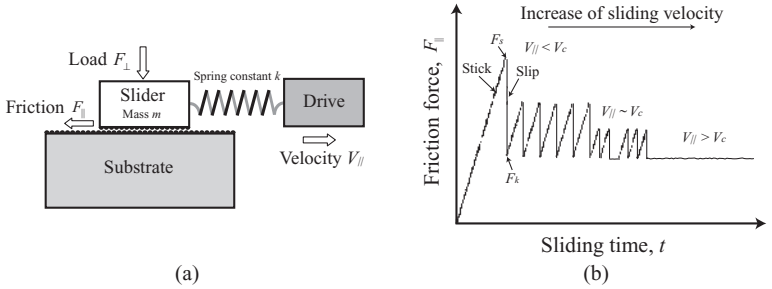


Figure 1.3 (a) A typical experimental setup for tribological studies and (b) a typical friction trace with stick-slip motion (when sliding velocity is below some critical value V_c).

higher static friction (μ_s) between the surfaces during the "stick" as compared to lower kinetic friction (μ_k) during the "slip" [47]. Based on their experiments on metals, Bowden and Tabor concluded that the occurrence of stick-slip motion depends on the type of metallic surfaces, the friction speed properties of the system, and the sliding velocity. Generally stick-slip is more commonly observed for dissimilar metals and metal combinations which show a large difference between μ_k and μ_s and at lower sliding speeds. As the sliding velocity increases, the time during which the surfaces remain together at the "stick" is reduced and the difference between μ_k and μ_s becomes less, which is accompanied by the decrease in the size of the fluctuations [47]. It should be noted that most of the instruments used in friction studies were assemblies of slider–spring where the friction force was measured by the deflection of the spring. It was argued that at least part of the stick-slip motion could be due to the dynamic instability of the mechanical apparatus rather than the genuine friction force generated between the surfaces [100, 101].

Another mechanism proposed for stick-slip dry friction is the surface topography model, which attributes the stick-slip motion to the surface roughness. As the slider rises an asperity, friction force is increased (stick), and after it reaches the peak of the asperity, it slides down the valley rapidly (slip). Such topographical stick-slip motion has been observed experimentally at the molecular level using AFM [76].

The distance-dependent model or creep model suggests that during shearing, a characteristic length D_c should be moved before adhesive junctions break (stick) and then the surfaces continue to slide with a lower friction force (slip) than the original force, and after that new contacts would form. The distance-dependent model also suggests a characteristic time τ_c is needed for adhesion and friction forces to increase after each new contact is made. This model has been used to analyze the stick-slip motion of various systems such as paper–paper and steel–steel. It was suggested that the distance-dependent model can also be applied to molecularly smooth surfactant or polymer surfaces as well [102].

Another proposed mechanism considers both intermolecular forces and mechanical instability of the spring during stick-slip friction. When two surfaces slide over each other under dry conditions with the slider attached to a spring, the total potential energy of the system can be considered as the sum of the intermolecular potential energy and the potential energy of the spring. The stick-slip motion can then be analyzed as the change in total potential energy of the system during sliding, which depends on spring constant, sliding velocity, and energy transfer mechanisms of the system. Therefore, in situations where the shear force is a constant force (i.e., no minima in the potential energy of the system), such as sliding down an inclined plane, stick-slip motion will not occur [7].

The above proposed mechanisms for stick-slip sliding are based on dry friction experiments where there is no lubricant between the surfaces. Experimental results show that stick-slip motion also occurs during sliding of lubricated surfaces [47, 103–105]. In this case, the frictional behavior of the surfaces depends on the thickness of the confined liquid film, which in turn is related to the applied normal load. As the thickness of the liquid film decreases, the friction force increases (see Section 1.6 for more details about different lubrication regimes). The friction force also increases with the viscosity of the film. Physical properties of molecularly thin liquid films can be very different from their bulk values due to ordering of the liquid molecules confined between the surfaces. For example, viscosity of the confined film can be orders of magnitude higher than the bulk viscosity since the liquid molecules are compacted between the surfaces [7, 106]. The stick-slip motion in the presence of a lubricant is usually due to periodic transitions between the "solid-like" and "liquid-like" states of the confined lubricant molecules and film corresponding to the "sticking" and "slipping" regimes, respectively [103–105]. However, it should be noted that occurrence of stick-slip motion during lubricated friction depends on many parameters such as type of lubricant and its molecular dimensions, type of interacting surfaces, nature of the intermolecular forces between the surfaces and between the surface and the lubricant, normal load, sliding velocity, as well as the inertia (stiffness and mass) of the tribological system. The stick-slip motion in lubricated friction is normally velocity dependent and disappears above some critical driving velocity (V_c) where the melted film would not be able to resolidify during the sliding (see Fig. 1.3b).

For more complex boundary lubricants such as surfactant layers and high MW polymer melts, the friction trace can have several maxima and minima at different sliding velocities, leading to several smooth and stick-slip regimes. Generally, three regimes can be considered for such systems:

(1) At very low sliding velocity ($V_{||} \sim 0$), the film behaves like a liquid, friction is low ($F_{||} \sim 0$) and the system is at thermodynamic equilibrium during sliding.

(2) At very high sliding velocity $V_{||}$ the lubricant chains have no time to interdigitate and the film behaves like a solid giving rise to low friction force $F_{||}$.
(3) At the intermediate regime, the sliding velocity $V_{||}$ is low enough that chain interdigitation occurs but not high enough to break the bonds and therefore high energy dissipation occurs, leading to high friction force $F_{||}$. Therefore, the stick-slip friction is expected at some critical velocity in the intermediate regime where energy dissipation is maximum and friction is high [7].

1.4.4 Directionality of Friction

The topography, structure, and alignment of the two surfaces moving against each other have a significant impact on the friction force, as evident from the dependence of friction force on the sliding direction, which is known as directionality. One of the well-known examples of directionality is the use of a saw where the force needed to pull or push depends on the direction. The directionality of friction at the molecular scale has been observed experimentally for several materials. For example, for mica surfaces it was found that the friction force depends on the mismatch angle between the two contacting cleavage lattices [80]. The friction force increased when the two mica surfaces formed commensurate structures and decreased along the mismatched lattices direction (also see Section 1.2.2 for discussion about surface energy of metals and crystalline materials). Friction directionality has been reported for lipid bilayer films which was attributed to different molecular alignments [107]. Very recently, friction anisotropy was also reported for exfoliated monolayer graphene by friction force microscopy [108].

1.5 ROLLING FRICTION

The beginning of the industrial revolution was accompanied by expansion of railways and wide usage of rolling bearings in different machines and mechanical systems. This vast presence of rolling elements brought about another subject of study, namely rolling friction. Although it has been long established that rolling friction is far less than sliding friction, the first quantitative study of rolling friction was done by Coulomb. Coulomb's experiments on the rolling of wooden cylinder over a flat wooden surface resulted in the relation shown in Equation 1.59,

$$F_{\text{rolling}} = k_O \frac{F_{\perp}}{R}, \tag{1.59}$$

where $F_{\perp}$ is load, R is radius of roller, k_O is a constant, and F_{rolling} is rolling friction force. It was believed that in rolling friction, similar as in sliding

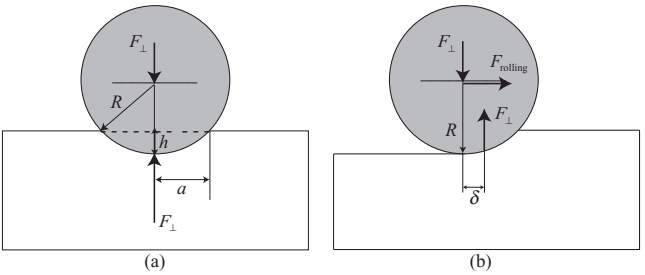


Figure 1.4 Dupuit's theory of rolling friction. (a) A cylinder under applied load $F_\perp$ against a flat surface before motion and (b) after rolling motion starts.

friction, the surface asperities are responsible for resistance to motion. In 1839, Dupuit proposed another relation for rolling friction, as shown in Equation 1.60 [1]:

$$F_{\text{rolling}} = k_O \frac{F_\perp}{R^{1/2}}. \tag{1.60}$$

According to Dupuit's theory, when a cylinder rolls on a flat surface, the rear portion of contact region does not contribute fully to the ground reaction force as a result of deformation. Therefore, the ground reaction is acted in front of rolling axis as shown in Figure 1.4b.

The resisting couple ($F_\perp \delta$) should be overcome by the drawing torque ($F_{\text{rolling}} R$) before cylinder starts moving. Thus,

$$F_{\text{rolling}} R = F_\perp \delta,$$

or

$$F_{\text{rolling}} = \delta \frac{F_\perp}{\text{R}}. \tag{1.61}$$

For a cylinder compressed against softer material, the relation between penetration depth h and the radius of contact zone a is given by:

$$a^2 \approx 2Rh. \tag{1.62}$$

Dupuit assumed that location of ground reaction δ is proportional to the arc of contact such that:

$$\delta \propto a \propto (Rh)^{1/2}. \tag{1.63}$$

Replacing the δ in Equation 1.61 by Equation 1.63 would result in Equation 1.60. The main drawback of Dupuit's theory is that depth of penetration h was assumed to be only a function of the material properties and independent of the load. According to Dupuit's theory, the contact radius a is also independent

of the load and determined solely by the radius of the cylinder, which is in contrast to elastic deformation of solids. For example, in Hertz' theory of elastic contact, for a cylinder on a flat surface, the contact radius is proportional to $F_{\perp}^{1/2}R^{1/2}$, which would result in Equation 1.64 for rolling resistance of a cylinder on a plane based on Dupuit's theory (Equation 1.61):

$$F_{\text{rolling}} = k_O \frac{F_{\perp}^{3/2}}{R^{1/2}}. \tag{1.64}$$

The mechanism of rolling friction depends on whether a material is elastic or plastic. It should be noted that for a material in the elastic regime, when the load is removed, the material will return to its original undeformed state, but the plastic regime is accompanied by permanent deformation of the material. For example, if the friction of two surfaces occurs in the elastic regime, the initial surface topography can be recovered, but with plastic deformation, a permanent change in surface topography will take place, which can change interfacial friction behavior. Bentall and Johnson showed that Equation 1.64 is valid for elastic regime but the analysis becomes more complex for viscoelastic and plastic regimes [109]. Modern theories mostly attribute the rolling friction to deformation losses [110] when the material is plastic, and to hysteresis losses [111] when it is in elastic regime.

1.6 LUBRICATION

The importance of lubrication had been realized by early civilizations when they used mutton or beef tallow to lubricate chariot wheels or when they used oil to help the passage of sledges over planks [1]. For a long period of time, vegetable and animal oils such as whale oil, fish oil, or olive oil were the only lubricants used. Industrialization, development of the railways, and textile industry replaced these traditional lubricants by mineral oil from shale or from wells. Soon afterwards, lubrication system became an essential part of any machinery. However, the knowledge about lubrication mechanisms remained primitive until the middle of nineteenth century. Since friction was known to be related to the roughness of surfaces, it was believed that lubricants could affect surface topography to reduce friction.

Petrov was the first who conducted systematic experiments to understand the hydrodynamic essence of lubrication. In 1883, Petrov studied the lubrication of two concentric cylinders with a film of lubricant in between. To account for slip between the lubricant and the solid surfaces, Petrov applied the relation proposed by Navier shown in Equation 1.65 [1],

$$\tau = \alpha_f v, \tag{1.65}$$

where τ is the shear stress at fluid–solid interface, α_f is the coefficient of external friction, and v is the relative velocity between the fluid and the solid at the

interface. For friction between layers of fluid he used Newton's law of viscosity:

$$\tau = \eta \frac{du}{dn}, \tag{1.66}$$

where τ is internal shear stress, η viscosity of the fluid and du/dn is the normal velocity gradient. Applying Equation 1.65 and Equation 1.66, Petrov proposed the following relation for friction force $F_{\|}$ [1]:

$$F_{\|} = \frac{2\pi r_i L \eta V_{\|}}{\left[D + \left(\frac{\eta}{\alpha_i}\right) + \left(\frac{\eta}{\alpha_o}\right)\right]}, \tag{1.67}$$

where D is the thickness of the lubricating film $D = r_o - r_i$, r_i and r_o are radii of the inner and the outer cylinders, respectively, L is the length of cylinders, α_i and α_o are the coefficient of external friction as defined in Equation 1.65 of the inner and outer cylinders, respectively, and $V_{\|}$ the relative velocity of rotation of inner cylinder. In the limiting case of no slip at the fluid–solid interface, Equation 1.67 reduces to:

$$F_{\|} = \frac{\eta V_{\|} A}{D}, \tag{1.68}$$

where A is the inner cylinder surface area $2\pi r_i L$. Equation 1.68 is also valid for lubrication between two flat parallel surfaces, which is another example where Amontons' laws are not valid since the friction force is directly proportional to the sliding velocity $V_{\|}$ and area A. Therefore, coefficient of friction μ for no-slip condition would become:

$$\mu = \frac{F_{\|}}{F_{\perp}} = \frac{\eta V_{\|} A}{D F_{\perp}}, \tag{1.69}$$

where $F_{\perp}$ is the applied load.

Soon after Petrov, in England, Tower constructed a machine to study friction and lubrication in the bearings. Tower accidentally discovered that there is a pressure gradient in the oil film surrounding the bearing. This finding was a great turning point in the history of tribology which stimulated the theoretical work by Osborne Reynolds on fluid-film lubrication [1]. In 1886, Reynolds published a classic paper on theory of lubrication [112] by applying general equation of motion, Newton's law of viscosity, and the corresponding boundary conditions to obtain pressure, velocity, and stress profiles in lubricant film for different geometries such as parallel surfaces in relative tangential motion. In the same paper, Reynolds also investigated the effect of temperature, load, and velocity on the performance of journal bearing. Reynolds concluded that metallic contact between journal and bearing occurs during the start of the motion of journal which is accompanied by abrasion and release of small solid

particles. These solid particles are responsible for blackening of lubricant and further wear in the system. It was suggested that impurities in the lubricant, the velocity of the journal, and the difference between axis of the journal and axis of the bearing will accelerate the rate of wear. Reynolds' theoretical analysis of lubrication matched very well with experimental data, which formed the basis of fluid-film bearing design for many decades to come.

Another mode of lubrication was reported by Hardy and Doubleday in 1922. This new form of lubrication was called *boundary lubrication* by Hardy. In boundary lubrication, the thickness of lubricant is in the order of size of the molecules as opposed to fluid-film lubrication, where the surfaces are completely separated by the lubricant film. It was shown in Hardy and Doubleday's systematic experiments that even very thin films of lubricant can reduce the friction between two surfaces extensively [113, 114]. Hardy and Doubleday measured the static coefficient of friction for three different solid surfaces (glass, steel, and bismuth) using different lubricants (alcoholic and paraffinic). According to their results, friction between two surfaces depends on type of lubricant, nature of solid surfaces, and MW of lubricant. For both types of lubricants, the coefficient of friction reduced with lubricant MW. Hardy suggested that molecules of lubricant form a monolayer on the solid surfaces and mask their field of force. Therefore, as the MW of lubricant increases, the distance between the solid surfaces also increases, which diminishes the interacting force between the surfaces. The efficiency of the lubricant also depends on the strength of adhesion of lubricant molecules on the solid surface, which in turn depends on the intermolecular forces between lubricant molecules and the solid substrate. It should be reminded that based on Coulomb's theory, interlocking of surface asperities was responsible for friction between two surfaces and the effect of a lubricant was to separate these asperities. For the first time, in Hardy's study, the role of intermolecular forces on the friction between two surfaces was being systematically investigated.

For boundary lubrication of solid surfaces, wear of the sliding surfaces was always reported [47]. The wear observed suggests that boundary friction cannot be simply the result of sliding of lubricant monolayers over each other. Bowden and Tabor proposed another mechanism of boundary lubrication, which states that the friction force is due to both the shear of metallic junctions and lubricating film [47]. The boundary lubrication mechanisms proposed by Hardy, Bowden, and Tabor are shown schematically in Figure 1.5. In Figure 1.5, A is the contact area and αA is the area where lubricant monolayer is broken under the load and intimate metallic junction occurs.

Based on Bowden and Tabor's theory, the role of lubricant is to inhibit intimate metallic contact between the surfaces. Thus, a good lubricant should not only adhere well to the substrate surfaces, but also have strong (lateral) adhesion between hydrocarbon chains to prevent monolayer breakdown. Two commonly used methods for producing monolayers are Langmuir–Blodgett (LB) deposition and chemical grafting of molecules into self-assembled monolayers (SAMs). Lubrication experiments done by AFM and friction force

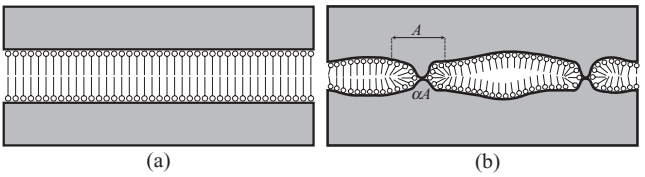


Figure 1.5 Mechanisms of boundary lubrication proposed by (a) Hardy, in which friction force is only due to interaction of lubricant monolayers; and by (b) Bowden and Tabor, in which friction is due to shear of metallic junctions and lubricant monolayers. (Reprinted from Bowden, F.P., Tabor, D. (1950) *The Friction and Lubrication of Solids. Part I*. Oxford University Press. © Oxford University Press.)

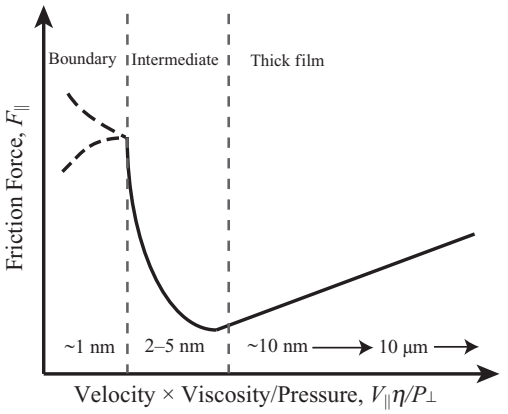


Figure 1.6 A typical Stribeck curve showing three regimes of lubrication or lubricated friction and the corresponding film thicknesses. (Reprinted from Israelachvili, J.N. (1999) Surface forces and microrheology of molecularly thin liquid films. In: *Handbook of Micro/Nanotribology*, ed. Bhushan, B. CRC Press, Boca Raton, FL, chapter 9, p. 27. © CRC Press.)

microscope (FFM) (see Section 1.9 for equipment details) revealed that SAMs are more effective in reducing the coefficient of friction and have greater durability in comparison with LB films [115]. SAMs are normally chemically grafted to the substrate through strong covalent bonds while LB films are usually bonded by weak VDW attraction. Thus, by choosing appropriate chain length and terminal linking group of SAMs, it is possible to achieve effective and optimized lubrication for various applications.

With the development of fluid-film lubrication and boundary lubrication models, the question that remained unclear was under what condition each model would play the important role. The experimental study by Stribeck on friction of journal bearings resulted in an empirical curve which is now well known as the "Stribeck curve" and shows different lubrication regimes. A typical Stribeck curve is shown in Figure 1.6.

The three lubrication regimes in the Stribeck curve are boundary lubrication regime, intermediate or mixed lubrication regime, and fluid-film lubrication regime. The corresponding film thickness for each of these regimes is also shown in Figure 1.6. The boundary and fluid-film lubrication regimes have been previously discussed briefly. The intermediate regime is normally accompanied by an increase in viscosity and non-Newtonian flow behavior. The rheological properties of a film in the intermediate regime are between that of the bulk and boundary properties.

The conventional research in tribology mostly focuses on machines and mechanical devices. A comparatively new research area in the field is the study of lubrication and friction processes in biological systems or so-called biolubrication [116–120]. One of the main differences is that conventional lubricants are oil based while biological lubricants are water based [4]. Joints, tissues, motion of blood cells in blood capillaries, and rapid movement of gecko on walls are all examples of biological systems in which friction and lubrication processes play important roles. A thorough understanding of these tribological processes in biological systems is greatly needed to help develop biolubricants which can be used in biomedical implants and nano-/microbiomedical devices.

1.7 WEAR

From a chronological point of view, scientific studies of wear followed that of friction and lubrication, which was partly because engineers focused more on the *functioning* of machines and moving parts rather than their lifetime and long-term *reliability*. Wear is loss of material from substrate surfaces as a result of their relative motion at the interface. When two surfaces come into contact, the nature of interfacial junctions formed determines their tribological behavior. While at first sight wear might appear to be proportional to friction, generally there is no direct relation between the friction coefficient and the amount of wear of different materials. For example, studies of Bowden and Tabor on metals showed that the amount of wear could be negligible while the friction coefficient was high and vice versa, which depended on the strength of the metallic junctions, nature of sliding metals, and possible oxide films present [47].

Early investigations on the wear of metallic surfaces revealed several important aspects of wear. First, for a constant load, wear was found to be directly proportional to the distance traversed. Thus, the amount of wear is usually shown in mass loss per unit of distance traversed. Second, similar to all other tribological phenomena, the amount of wear is considerably affected by a thin layer on the material surface. For example, it was found that a thin layer of hard metals such as rhodium or chromium can significantly reduce the wear between metallic surfaces. These hard metals (e.g., rhodium, chromium) are hardly worn by other metals. Moreover, chromium oxide film is strongly

attached to the chromium surface, which prevents intimate metallic junction. Tabor did a set of wear measurements between a chrome molybdenum steel surface and a cast iron hemispherical slider coated with a film of chromium. He found that if the thickness of the chromium layer on the cast iron slider exceeded 5 μm then the amount of wear would decrease to 0.005 μg/cm from an initial value of 4 μg/cm [47]. The surrounding atmospheric conditions (i.e., temperature, humidity, and chemical composition) can also significantly influence the amount of wear. For example, the presence of oxygen in the atmosphere normally results in the formation of oxide films on metallic surfaces. The presence of the oxide film, in turn, will affect the wear. If the oxide film is strongly attached to the underlying metal, as in the case of Al_2O_3 to aluminum, it will act as an abrasive surface and cause heavy wear on steel, for instance, because Al_2O_3 crystals are much harder than iron oxides. Contrarily, if the oxide film is soft, the amount of wear would be relatively small [47].

Understanding the mechanisms of wear in practical application can assist in its reduction. The most common mechanisms of wear include: *adhesive*, *abrasive*, *corrosive*, *erosive*, and *fatigue*, which are discussed in the succeeding paragraphs.

As mentioned earlier, when two solid surfaces are placed into contact, adhesion takes place at the interfacial junctions formed. When a tangential force is imposed, the adhesive junctions should be broken to allow the tangential motion to occur. Depending on the nature of the adhesive junctions, the rupture can occur either at the interface or at the surface of the cohesively weaker material. As a result, part of the cohesively weaker material transfers to the cohesively stronger material. This process is known as *adhesive wear* because it takes place as a result of adhesion at the interface. Adhesive wear is the most common type of wear among rubbing metals. Many experiments in the 1950s showed that adhesive wear is directly proportional to the distance traversed and the normal load, and inversely proportional to the hardness of the softer material. However, it has been noted by many researchers that there are many exceptions to the above mentioned relation [1].

In *abrasive wear*, hard asperities or debris that are in relative motion with a softer surface can cause abrasion of the surface. This type of wear is used in many industrial applications for cutting, grinding, and polishing of many materials. For example, aluminum oxide or silicon carbide powders, which are materials with high cohesive energy, are widely used for the polishing of surfaces [20]. As a result of abrasive wear process, the surface roughness of the polished surfaces would decrease. However, abrasive wear process can be harmful to operating machinery such as gears, bearings, and mechanical seals. Adhesive and abrasive wear mechanisms have been shown to play important roles in chemical mechanical polishing (CMP) processes.

Corrosive wear occurs when chemical or electrochemical reaction is accompanied with relative motion of a surface. Corrosion can take place on many materials, especially metallic surfaces. The process in which the corrosion products are removed as a result of the relative motion of surfaces is known as corrosive wear. Because of the chemical nature of corrosive wear process,

environmental conditions such as temperature, pressure, and chemical composition can significantly affect the rate of wear process. For example, the presence of oxygen or corrosive compounds in the lubricants can usually trigger corrosive wear. Similarly high friction coefficient commonly results in higher temperature at the interface to promote the chemical reactions.

Erosive wear occurs when a particle (solid, liquid, or gas) impinges a surface which results in loss of material from the surface. Along the nature of particle and surface, impingement velocity and angle are also important factors in determining the rate of erosive wear. Some studies have tried to reveal the role of cohesive energy of a material in the rate of erosive wear. For metals, it was found that as the binding energy of metal–metal bonds increases, the amount of erosive wear would decrease [20].

When a material undergoes cyclic loading–unloading, localized structural damage will occur gradually. This process is called fatigue, and loss of material as a result of this process is known as *fatigue wear*. Fatigue is usually accompanied by formation of cracks on the surface or subsurface region. Progression of these cracks will eventually generate wear particles. Generally, as the number of cycles increases, the probability of fatigue wear also increases.

1.8 REAL CONTACT AREA

In practice, a completely flat surface does not exist. Any real surface has some peak-and-valley pattern which is detrimental in its tribological behavior. When two solid surfaces are brought into contact, they are connected to each other through these irregularities, and their real contact area is normally far less than the apparent contact area. Thus knowledge about the topography of surfaces is a priority for tribological studies. Many methods have been developed through the past decades for topography analysis of the surfaces such as optical interference, electron microscope, and AFM, some of which will be discussed in the next section.

As mentioned earlier, when two surfaces come into contact, they contact each other through the peaks of asperities, and at the points of intimate contact these asperities can undergo plastic deformation readily while the bulk of the material do not deform. As load increases, the intimate contact area between the asperities will increase to distribute the load over larger area, and elastic deformation in the bulk of material starts. Further increase in the load will result in plastic deformation of both the asperities and the bulk of the material, although each asperity may still retain its identity. The analysis by Bowden and Tabor [47] showed that for any type and shape of surface asperities, the real contact area is almost proportional to the load:

$$A_{\text{real}} = \frac{F_{\perp}}{P_m}, \tag{1.70}$$

where P_m is the mean yield pressure of the asperities (yield pressure is the limit of elastic regime above which material undergoes plastic deformation).

According to Hertz's theory of elastic deformation, contact area is proportional to $F_{\perp}^{2/3}$ and this might seem contradictory with Equation 1.70. However, it should be noted that as soon as the surfaces are brought into contact, plastic deformation of the surface asperities occurs and the real contact area increases proportionally with load, while the bulk of material deforms elastically and the apparent contact area increases with $F_{\perp}^{2/3}$. This trend continues until the onset of plasticity in the bulk of the material. Greenwood and Williamson argued that the deformation in the real contact area does not necessarily need to be plastic [52]. They proposed a statistical model for the topography of rough surfaces (see Section 1.3.7) and provided a criterion, the plasticity index, ψ, to determine whether the intimate contact is elastic or plastic:

$$\psi = \frac{E'}{H}\sqrt{\frac{\sigma}{\beta}}, \tag{1.71}$$

where $1/E' = (1-\nu_1^2)/E_1 + (1-\nu_2^2)/E_2$, H is hardness, σ here is the standard deviation of the height distribution of asperities, and β is the radius of curvature of asperities. The plasticity index ψ combines the material and topographic properties of the solids in contact. The deformation of asperities is elastic for $\psi < 1$ and plastic for $\psi > 1$. Many similar statistical models have been proposed afterwards [121–125]. The ratio of the real contact area to the apparent contact area also depends on the geometry of the surfaces, which could be as high as 1:2 for a cylinder on a grooved surface or as low as 1:100,000 for two flat surfaces [47].

Different methods have been developed for the measurement of real contact area. Three of these methods are briefly reviewed as follows. In 1939, Bowden and Tabor did a classic experiment to investigate the real contact area through the measurement of electrical resistance between two conducting surfaces [126]. Suppose that two conducting surfaces are brought into contact with the radius of contact area of a, which is very small compared to the size of the surfaces. If electric current is passed through the contact area, as a result of constraint in the flow of current stream, an electric resistance called *spreading resistance* (R_{Ω}) will be given by:

$$R_{\Omega} = \frac{1}{2a\Pi}, \tag{1.72}$$

where Π is the electric conductivity of the material. Therefore, by measuring the electric resistance and knowing the value of electric conductivity, the real contact area can be determined. One limitation of this method is that it can be used mainly for conductive surfaces which can pass electric current easily such as metallic surfaces. It should be noted that even for metallic surfaces, the formation of oxide layers on the surfaces can complicate the data analysis [47].

Another method to determine the real contact area is mainly based on Equation 1.70. Assuming plastic flow, the yield pressure (P_m) can be measured

by indentation experiments and real contact area can be then calculated as a function of applied load based on Equation 1.70.

The third method is based on optical interferometry by using polarized white light [127, 128]. When two surfaces are brought into contact and white light is passed through them, the interference fringes in the real contact area would be dark based on optical path difference of reflected light. The real contact area can be then determined by an image processing method on the interference pattern.

1.9 MODERN TOOLS IN TRIBOLOGY

All tribological phenomena occur on material surfaces. Characterization of the surface properties of materials is needed for in-depth understanding of their tribological phenomena. Various techniques have been developed for the chemical and topographical characterization of material surfaces. A brief overview of some of the most widely used techniques for surface analysis and tribological studies are discussed in the succeeding sections.

1.9.1 X-Ray Photoelectron Spectroscopy

X-ray photoelectron spectroscopy (XPS) is also known as electron spectroscopy for chemical analysis (ESCA). XPS has been used extensively for chemical analysis of material surfaces which gives quantitative information on elemental composition of the surfaces. Following the early experiments by P.D. Innes, Moseley, Rawlinson, and Robinson on photoelectric effects, Kai Siegbahn and his group at the University of Uppsala in Sweden made significant progress in developing the XPS techniques in the 1950s and 1960s [129]. XPS measurements require ultra-high vacuum (UHV) conditions. In a typical XPS measurement, a source of X-ray generates and impinges X-ray photoelectrons on the material surface, which excite the electrons of atoms on the surface and cause them to leave the surface. The kinetic energy and number of the excited electrons are measured by a detector. The kinetic energy of the excited electron is directly related to its binding energy—the energy of an electron bounded to a particular atom, which also depends on the chemical group which the atom is attached to. Thus, by measuring the binding energy of the excited electrons, information about the chemical nature of the surface can be obtained, which is important for understanding many tribological phenomena. The probing depth of XPS ranges from 1 to 12 nm, which makes it suitable for chemical analysis of solid films and surfaces.

1.9.2 Scanning Electron Microscopy

Scanning electron microscope (SEM) is a powerful tool for studying surface topography, electrical conductivity, and fracture pattern of material surfaces,

which provides excellent physical picture of materials surfaces in various tribological studies. In a typical SEM measurement, an electron beam is emitted from an electron source and then accelerated and focused on a specimen surface. After the electron beam hits the surface, energy exchange occurs between the electron beam and the sample surface and results in the emission of secondary electrons, which are common in all SEMs. The emitted secondary electrons strike the detector and the resulting signal is amplified and displayed as brightness of the cathode ray tube. It should be noted that other types of signals can also be generated by an SEM which include backscattered electrons, characteristic X-rays, light, specimen current, and transmitted electrons. For example, SEM images using the signal of backscattered electrons can provide information about the distribution of different elements on the specimen surface, as the signal intensity of backscattered electrons is strongly related to the atomic number of the specimen. SEM can also provide useful information about the crystalline nature of solids, which can be used for analyzing surfaces in tribology [20].

1.9.3 Infrared Spectroscopy

Infrared spectroscopy (IR) has been widely used for characterizing the chemical structures of monolayers, chemisorbed species, and substrate surfaces in various tribological studies. IR is based on the fact that each molecule or chemical bond absorbs specific frequencies of light which are characteristic of their chemical structure. Absorption occurs when the IR frequency matches the vibrational frequency of a bond and therefore valuable information on the chemical structure of materials can be obtained.

1.9.4 Optical Tweezers or Optical Trapping

Optical tweezers (OT) employ radiation pressure to measure interaction forces between two particles, which have been also used to study the interactions of polymers and biomacromolecules. Electromagnetic radiation exerts forces upon any surface exposed to it, which is known as radiation pressure, and was first deduced theoretically by James Klerk Maxwell in 1871. In OT, a small particle can be trapped by the radiation pressure via a highly focused laser beam to generate forces on the particle, of which the size can range from ~10 μm [130, 131] down to atomic levels [132]. In a typical OT measurement, the applied force ranges from 1 to ~1000 pN, and the deflection of the laser beam is used to measure the distance/displacement with a typical resolution of ~1 nm. However, the use of laser beams in OT usually involves heating of the sample, which can be a limiting factor for biological samples due to their sensitivity to temperature. The distinctive feature of OT is the excellent control over the applied force which allows the best time-dependent control of forces between single molecules [133].

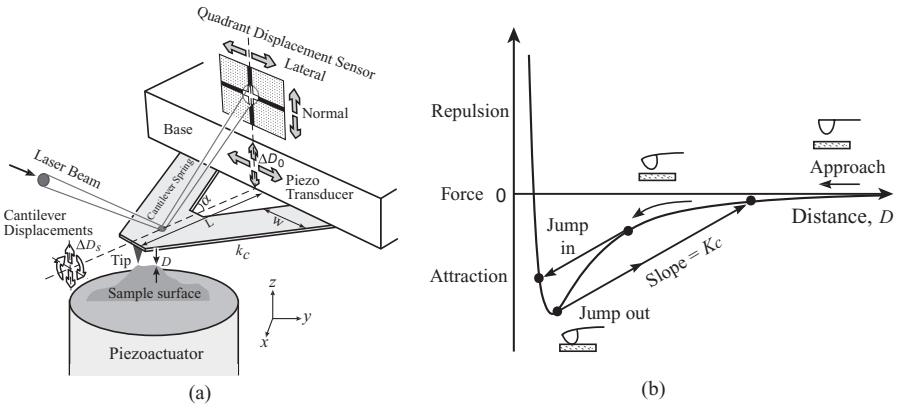


Figure 1.7 (a) Schematic of the working principle of an AFM and (b) typical normal force versus distance curve obtained using an AFM.

1.9.5 Atomic Force Microscope (AFM)

The first AFM was developed by Binnig, Quate, and Gerber in 1986 as a modified combination of the scanning tunneling microscope (STM) and the stylus profilometer, which was usually used for the study of surface roughness [134]. AFM has been extensively used to measure interfacial forces, surface adhesion and friction, as well as to characterize surface topography at the nano- and atomic scale. The basic key components of a typical AFM include laser diode, photodiode, cantilever and tip, piezoactuator or piezoelectric tube (PZT) scanner, and feedback control circuit. A schematic drawing of the working principal of AFM is shown in Figure 1.7a.

As shown in Figure 1.7, AFM consists of a flexible cantilever beam with a sharp tip at one end. The AFM cantilever is usually made of silicon or silicon nitride with typical spring constant of 0.01–100 N/m, and the radius of curvature of the tip is in the range of 5–100 nm. There are different methods to determine the spring constant of a cantilever. For a rectangular cantilever with cross-section of width of w, length L, thickness t_c, and Young modulus of E, a simple expression for calculation of the spring constant is [135]:

$$K_c = \frac{F}{Z_c} = \frac{Ewt_c^3}{4L^3}, \tag{1.73}$$

where F is the applied force to the end of the cantilever and Z_c is the deflection of the cantilever at its end. For a V-shaped cantilever, a commonly used expression for the spring constant is [135]:

$$K_c = \frac{Ewt_c^3}{2L^3}\cos\alpha\left[1+\frac{4w^3}{t_c^3}(3\cos\alpha-2)\right]^{-1}, \tag{1.74}$$

where α is the opening angle (see Fig. 1.7). The experimentally measured values for spring constant usually deviate from the theoretical values, which is normally due to the nonuniformity of the thickness of cantilever (t_c) and deviation of Young's modulus of a thin layer from that of the bulk material. Thus, it is always better to calibrate the spring constant of cantilever before force measurement. A general method to measure the spring constant is by applying a known force to the cantilever and then measuring its deflection to get the spring constant as $K_c = F/Z_c$. Another widely used method is based on the change in the resonance frequency when a known mass is attached to the end of the cantilever. For a rectangular cantilever, the spring constant is calculated as [135]:

$$K_c = \frac{4\pi^2 M}{1/\nu_0'^2 - 1/\nu_0^2}, \tag{1.75}$$

where ν_0 is the initial resonance frequency and ν_0' is the resonance frequency of the cantilever after mass M is attached. Hutter and Bechhofer proposed another widely used method to determine the spring constant of cantilever from the power spectral density of cantilever fluctuations due to thermal noise, which does not attach any mass and has been used in many models of commercial AFMs [136].

Forces as small as 10^{-11} N between an AFM tip and a sample surface can be detected by monitoring the deflection of the cantilever beam. Different techniques have been used for measuring the deflection of the cantilever beam, including optical deflection, optical interference, capacitance, and tunneling current [137]. Among these techniques, laser beam deflection technique is one of the most common methods used in commercial AFMs. As shown in Figure 1.7, a laser beam is directed toward the top surface of the cantilever near the tip, and the reflected laser beam is detected by a photodetector. The differential signal detected by the four quadrants of the photodetector provides a direct measurement of the cantilever deflection. The PZT used in AFM scanner is a piezoelectric material that can expand or contract when an electric voltage is applied, which has two main designs in an AFM system. In a small-sample AFM, a sample surface is mounted on a PZT scanner which can move the sample in x-, y-, and z-directions. In a large-sample AFM, the cantilever is mounted on a PZT scanner for the measurement of large samples, which normally has relatively lower lateral resolution than the design of small-sample AFM due to the vibrations generated by the cantilever movement [137].

AFM is widely used for the study of surface topography with two different imaging modes: contact mode and tapping mode. In contact mode, a feedback control mechanism is employed to adjust the distance between the tip and sample surface by regulating the voltage applied to the PZT scanner while keeping the cantilever deflection (or the force) constant. The movement of PZT scanner in the z-direction is thus a direct measure of the roughness of

the sample surface. In tapping mode imaging, the cantilever tip does not contact the sample surface but taps it. In this mode, the cantilever/tip assembly is vibrated sinusoidally at a frequency slightly higher than its resonance frequency (350–400 kHz). A feedback control system is used to maintain a constant oscillating amplitude of the cantilever/tip by adjusting the distance between the tip and the sample surface in the z-direction. Thus in tapping mode, set point is the constant oscillating amplitude of the cantilever. The feedback signal sent to the z-direction piezo to keep the set point constant provides a measure of the sample roughness. Imaging in the tapping mode generally causes less damage to the sample surface than in the contact mode, thus tapping mode is preferable for measuring topography of soft surfaces. The cantilever specifications for the tapping and contact modes are normally different. Contact mode imaging is based on controlling the force between the tip and sample surface, thus a relatively soft and sensitive cantilever (0.06–0.6 N/m) with low resonance frequency (13–40 kHz) is preferred. Tapping mode is based upon adjusting the oscillating amplitude of the cantilever/tip assembly, therefore a relatively stiffer cantilever (15–60 N/m) with higher resonance frequency (250–400 kHz) is more commonly used [137].

One of the major applications of AFM is to monitor the interfacial and adhesion forces. A typical force–distance curve obtained using AFM is shown in the illustration of Figure 1.7b. During the force measurement, the sample surface is moved toward the tip by the z-direction piezo at a constant velocity. When the sample and the tip are far away from each other, there is no force between them. As the cantilever tip is close to the sample surface (from 1 to >10 nm), the intermolecular and surface forces between the tip and sample result in the deflection of the cantilever. It should be noted that force–distance curves are usually normalized by dividing the force F by the radius of curvature of the surface R, as the absolute forces exerted between two surfaces are proportional to the interacting area (or number of molecules involved). As a result, the normalized forces F/R (with a unit of newtons per meter [N/m] or joules per square meter [J/m^2]) obtained in one experiment can be compared with theoretical values or other experiments.

There are two limitations or challenges which should be noted in AFM force measurements. First, the radius of curvature of the AFM tip is usually not well defined in AFM experiments as a result of difficulties during the manufacturing process [138]. Moreover, tip wear, which is the change in shape and/or size of the tip during force measurements, is one of the major problems with AFM force measurement that further complicates the determination of radius of curvature. To overcome this issue, SEM has been commonly used to characterize the size and shape of AFM tips before and after experiments. However, it should be noted that the tip surfaces need to be conductive for SEM imaging and the typical space resolution of SEM is of the order of 10 nm (although 1 nm resolution can be achieved in some cases) [135]. Second, the zero separation normally cannot be determined directly in AFM force measurements, and usually the linear part of the force curve in the contact regime

is assumed to be the zero separation. In most applications, this method will not cause any problem; but for highly deformable surfaces, soft materials, or for situations where strong repulsive forces are present, the interpretation of the results can become rather complicated.

AFM has been modified by utilizing a sensor which is capable of measuring lateral forces to be used as so-called friction force microscope (FFM) or scanning force microscope (SFM) [76]. The principle of FFM or SFM is the same as AFM: lateral forces cause bending and torsion of the cantilever which deflects a laser beam. The deflection of the laser beam is detected by photodiodes. However, the calibration of lateral forces (relationship between bending and torsion of the cantilever and the amount of force applied) is more complicated than just applying the Hook's law. For lateral force calibration, several parameters such as geometrical dimensions of cantilever, elastic modulus, tip height, position of the tip with respect to cantilever, and sensitivity of the photodiodes must be known. As an alternative, *in situ* calibration of lateral forces can be done using sample surfaces with well-defined profiles [137]. As has been discussed earlier in this chapter, for fundamental understanding of friction, wear, lubrication, and adhesion, it is necessary to appreciate mechanisms and processes at the nanoscale and molecular level. For example, the macroscopic contact between two surfaces is the result of microscopic or nanoscopic contact of many asperities at the interface. Therefore, it is important to study single asperity contact at the nanoscale. FFM is a modern tool that can be used in the nanoscale study of friction, lubrication, and wear. There are several specific advantages for FFM in nanotribology studies, including: (1) the contact area is very small which enables the measurement of localized friction force, (2) the apparent and the real contact area are mostly the same, and (3) purely elastic regime conditions can be achieved when loading forces are sufficiently low [138]. For example, for wear studies, a hard tip (usually diamond) can be mounted on a stiff cantilever beam and an area on a sample surface is scanned at various normal loads. Another example is the friction study on graphite surfaces using FFM, which revealed the "stick-slip" mechanism of friction at the atomic scale [73, 76]. The role of topography, atmosphere conditions, normal load, and sliding velocity on friction and wear can be all thoroughly investigated in the nanoscale by FFM. The effect of scanning directions on friction at micro- and nanoscales has been investigated. It was found that friction depends on scanning direction which originates from anisotropy in surface topography [137]. It was also found that nanoscratches are responsible for wear initiation [137]. Therefore, for zero-wear conditions, the surfaces should be free of nanoscratches and contact stresses must be lower than the hardness of the softer material in order to minimize plastic deformation. It was also found that water adsorption, temperature, and the formation of meniscus at the AFM tip play important roles in the adhesion and friction measurement of various materials and surfaces [137]. Briefly, AFM/FFM is a sophisticated tool which has helped researchers understand the atomic origin of many tribological phenomena, which will lead to more efficient engineering designs.

1.9.6 Surface Forces Apparatus (SFA)

The SFA was originally developed by Tabor, Winterton, and Israelachvili [139–141]. Since then, significant advances have been made on the SFA design and technique such as SFA Mk I, II, III, and SFA 2000, which have been widely used to measure both normal and lateral forces between surfaces in vapors and liquids in many engineering and biological systems, for example, VDW forces, electrostatic forces, adhesion forces, friction and lubrication forces, hydrophobic interactions, and specific and nonspecific biological interactions [142–146]. SFA is principally similar to AFM except that SFA measures interactions between two large surfaces while AFM measures interactions between a fine tip and a surface. It should be noted that the distances measured in SFA are absolute distances, as different from in AFM. The distance resolution in SFA is ~0.1 nm and force sensitivity is ~1 nN.

A section view through the center of an SFA 2000 chamber is shown in Figure 1.8a. The basic components of SFA 2000 are micrometers, upper disk holder, lower disk holder attached to force springs, and the main stage which contains single-cantilever spring. To manipulate the distance between the interacting surfaces, there are four levels of control which cover the angstrom to the millimeter range and their specifications are shown in Table 1.5.

SFA measures the interactions between two curved surfaces in a crossed-cylinder configuration, which locally corresponds to a sphere (of the same radius R) against a flat plane based on the Derjaguin approximation [7], which correlates the force $F(D)$ between the two curved surfaces and $E(D)$ the interaction energy per unit area between two flat surfaces:

$$E(D) = \frac{F(D)}{2\pi R}. \tag{1.76}$$

The distance is measured in SFA using an optical technique called multiple-beam interferometry (MBI) by employing fringes of equal chromatic order (FECO). Mica has commonly been used as a supporting substrate in SFA experiments due to its transparent and molecularly smooth nature (for basal plane). Other materials such as sapphire, silica sheets, and polymers have also been used as supporting substrates for SFA experiments [7].

SFA have been widely used in fundamental studies of various friction and lubrication processes. A section view of SFA 2000 with the attachments for friction and lubrication experiments is shown in Figure 1.8b. The motor on the friction device is able to move the upper surface at constant or variable speed with respect to the lower surface. There are two double-cantilever springs with appropriate strain gauges attached. When a lateral force is applied to the upper surface, the springs will deflect and forces can be monitored through the voltage signals from the strain gauges. A piezoelectric bimorph slider device as shown in Figure 1.8b can also be used in SFA to measure the friction or lubrication forces. During the experiments, a triangular input signal is applied to the biomorph slider device which allows the lower surface to

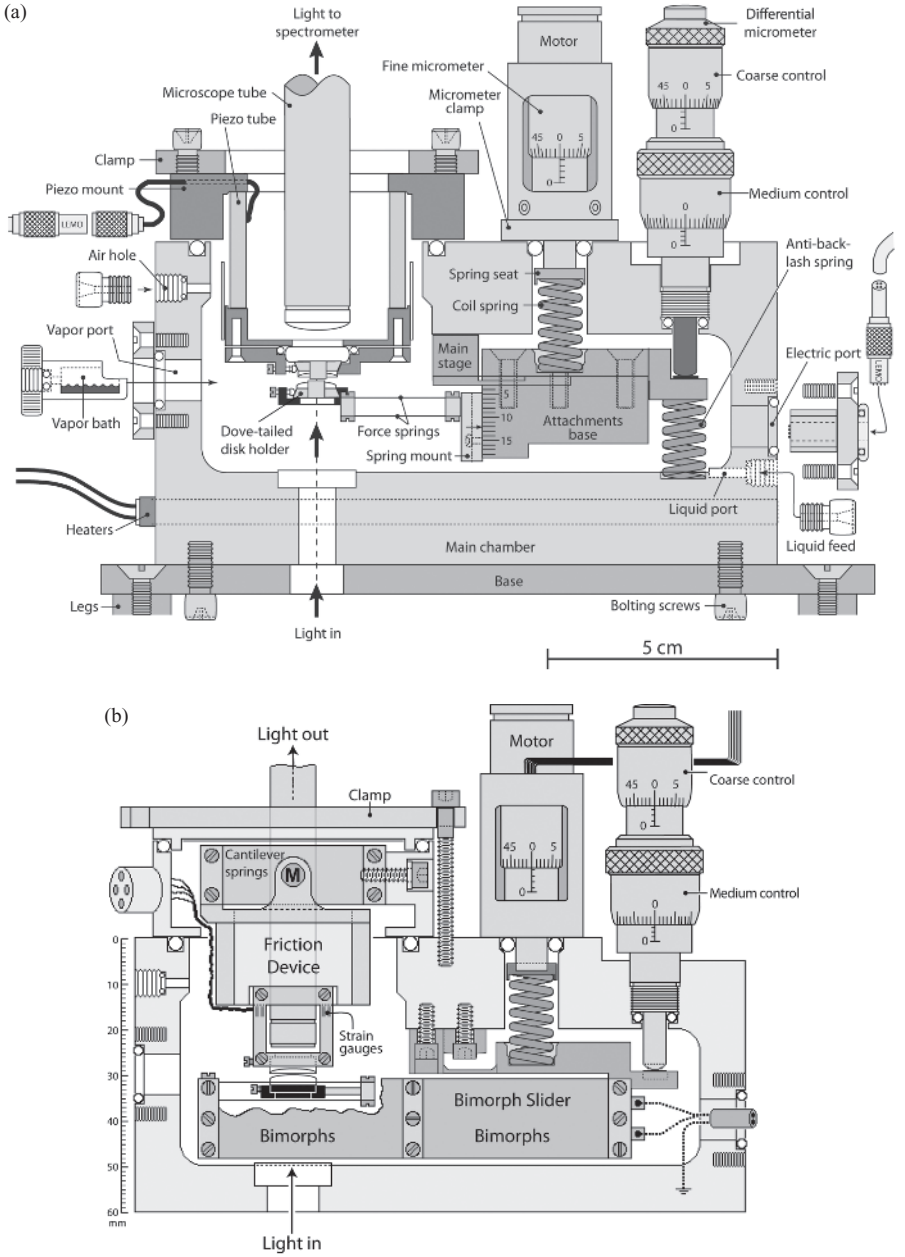


Figure 1.8 (a) A section view through the center of SFA 2000. (b) Side view of SFA 2000 with piezoelectric bimorph slider and friction device attachment. (Reprinted from Israelachvili, J., Min, Y., Akbulut, M., Alig, A., Carver, G., Greene, W., et al. (2010) Recent advances in the surface forces apparatus (SFA) technique. *Reports on Progress in Physics*, **73**, 036601. © IOP Publishing.) (See color insert.)

TABLE 1.5 Distance Controls and Their Specifications in SFA [142]

Level of Control	Type of Control	Positional Accuracy (Å)	Range of Movement (μm)
Coarse	Differential micrometer	2000	2000
Medium	Differential micrometer	500	200
Fine	Differential spring mechanism	2	10
Extra fine	PZT	<1	1

move at a constant speed laterally in both directions, while the friction force is still monitored through the top friction device.

Other techniques have also been developed to investigate the intermolecular and surface interactions, such as micropipette, osmotic stress and osmotic pressure techniques, total internal reflection microscopy (TIRM), and reflectance interference contrast microscopy (RICM). The main features of some commonly used techniques in tribological studies are summarized in Table 1.6, in which D is the distance or surface separation and ΔD is the relative displacement.

1.10 COMPUTER SIMULATIONS IN TRIBOLOGY

Rapid development of computer hardware and methodologies within the past two decades enables the study and modeling of tribological processes at the molecular scale. One of the most commonly used types of simulations is the molecular dynamics (MD) simulation. The basic principle and methodology of MD simulation have been extensively described in previous review articles and books [147–149]. Briefly, in MD simulations, an interaction potential is first defined between "particles" (typically atoms or molecules), and the forces exerted on each particle from all the other particles in the system is calculated. The initial and boundary conditions are specified and equations of motion for all particles are integrated and solved numerically. The computation is repeated in discrete time steps to get the trajectories of the particles in space and time. MD simulations have been used in molecular studies of many tribological processes, including adhesion and indentation [61, 150–153], the nature of stick-slip motion [105], the origin of friction [138, 150, 154–158], wear [138], and lubrication [159]. However, due to computational restrictions, MD simulations are currently limited to tens of nanoseconds of real time and dimensions of tens of nanometers, which have too short time and small dimensions of space compared to many real tribological processes [4]. In spite of all these advancements, fundamental questions such as the origin of energy dissipation associated with fiction, relationship between adhesion, friction, and wear, and a grand theoretical model for prediction of tribological processes under different experimental conditions are yet to be answered.

TABLE 1.6 Main Features of Some Commonly Used Techniques in Tribological Studies [133]

Technique	Typical Size of System, R	ΔF (N); $\Delta F/R$ (N/m)	Distance Resolution (nm), D, and $\pm\Delta D$	Features
Optical tweezers (OT)	Microscopic to molecular (0.1 nm–10 μm)	10^{-12} N; from 10^{-2} to 10^{-7} N/m	1 nm; ±0.1 nm	Provides high force sensitivity for adhesion and binding experiments, absolute separation distance (D) cannot be measured.
Surface forces apparatus (SFA)	Macroscopic (~10 mm)	10^{-9} N; 10^{-7} N/m	0.1 nm; ±0.1 nm	Measures absolute separation distance (D) and local geometry in situ, good for adhesion, friction and lubrication experiments.
Atomic force microscope (AFM)	Microscopic to molecular (–1 nm–10 μm)	10^{-11} N; 10^{-2} N/m (nano tip), 10^{-6} N/m (micro bead)	1 nm; ±0.1 nm	Good for adhesion and friction experiments, imaging surface topography. Cannot measure absolute separation distance (D),
Reflectance microscopy techniques (TRIM and RICM)	Microscopic (10 μm)	10^{-14} N; 10^{-9} N/m	1 nm; ±1 nm	Provides high force sensitivity, the systems are restricted, can only measure repulsive forces.
Micropipette aspiration and bioforce probe |(BFP)	Microscopic to molecular (0.1 nm–10 μm)	10^{-13} N or 10^{-6} N; 10^{-2} N/m or 10^{-6} N/m	1–5 nm; ±1–5 nm	Similar to reflectance microscopy techniques but the particle position can be controlled accurately, good for adhesion studies.
Thin film balance	Macroscopic to molecular (1 nm–1 mm)	N/A	1 nm; ±1 nm	Measures the interactions between thin film interfaces, stability of thin films, disjoining pressure of a thin film and the film thickness.

ACKNOWLEDGMENT

This work was supported by an NSERC Discovery Grant Award and an NSERC RTI Grant Award from the Natural Sciences and Engineering Research Council of Canada.

REFERENCES

[1] Dowson, D. (1979) *History of Tribology*. Longman, London.

[2] Hardy, W.B. (1936) *Collected Scientific Papers of Sir William Bate Hardy*. The Cambridge University Press, Cambridge.

[3] Akhmatov, A.S. (1966) *Molecular Physics of Boundary Friction*. Israel Program for Scientific Translations Ltd, Jerusalem, Israel.

[4] Urbakh, M., Klafter, J., Gourdon, D., Israelachvili, J. (2004) The nonlinear nature of friction. *Nature*, **430**, 525–528.

[5] Jost, H.P. (1990) Tribology—origin and future. *Wear*, **136**, 1–17.

[6] London, F. (1937) The general theory of molecular Forces. *Transactions of the Faraday Society*, **33**, 8–26.

[7] Israelachvili, J.N. (2011) *Intermolecular and Surface Forces*, 3rd ed. Academic Press Ltd, Burlington, MA.

[8] Derjaguin, B.V., Landau, L. (1941) Theory of the stability of strongly charged lyophobic sols and of the adhesion of strongly charged particles in solution of electrolytes. *Acta Physicochimica URSS*, **14**, 633–662.

[9] Verway, E.J.W., Overbeek, J.T.G. (1948) *Theory of Stability of Lyophobic Colloids*. Elsevier Publishing Co., Amsterdam, The Netherlands.

[10] de Gennes, P.G. (1987) Polymers at an interface; A simplified view. *Advances in Colloid and Interface Science*, **27**, 189–209.

[11] Christenson, H.K., Claesson, P.M. (2001) Direct measurements of the force between hydrophobic surfaces in water. *Advances in Colloid and Interface Science*, **91**, 391–436.

[12] Craig, V.S.J., Ninham, B.W., Pashley, R.M. (1999) Direct measurement of hydrophobic forces: A study of dissolved gas, approach rate, and neutron irradiation. *Langmuir*, **15**, 1562–1569.

[13] Christenson, H.K., Claesson, P.M. (1988) Cavitation and the interaction between macroscopic hydrophobic surfaces. *Science*, **239**, 390–392.

[14] Tsao, Y., Evans, D.F., Wennerstrom, H. (1993) Long-range attraction between a hydrophobic surface and a polar surface is stronger than that between two hydrophobic surfaces. *Langmuir*, **9**, 779–785.

[15] Israelachvili, J.N., Pashley, R.M. (1984) Measurement of the hydrophobic interaction between two hydrophobic surfaces in aqueous electrolyte solutions. *Journal of Colloid and Interface Science*, **98**, 500–514.

[16] Craig, V.S.J., Ninham, B.W., Pashley, R.M. (1993) Effect of electrolytes on bubble coalescence. *Nature*, **364**, 317–319.

[17] Attard, P. (2003) Nanobubbles and the hydrophobic attraction. *Advances in Colloid and Interface Science*, **104**, 75–91.

[18] Stone, A.J. (1996) *The Theory of Intermolecular Forces*. Oxford University Press, Oxford, UK.

[19] Langmuir, I. (1933) Surface chemistry. *Chemical reviews*, **13**, 147–191.

[20] Buckley, D.H. (1981) *Surface Effects in Adhesion, Friction, Wear, and Lubrication*. Elsevier Scientific Pub. Co., Amsterdam, The Netherlands.

[21] Fox, H.W., Zisman, W.A. (1952) The spreading of liquids on low-energy surfaces. II. Modified tetraflouroethylene polymers. *Journal of Colloid Science*, **7**, 109.

[22] Fox, H.W., Zisman, W.A. (1952) The spreading of liquids on low-energy surfaces. III. Hydrocarbon surfaces. *Journal of Colloid Science*, **7**, 428–442.

[23] van Oss, C.J., Chaudhury, M.K., Good, R.J. (1987) Monopolar surfaces. *Advances in Colloid and Interface Science*, **28**, 35–64.

[24] Hertz, H.R. (1896) Miscellaneous papers.

[25] Griffith, A.A. (1921) The phenomena of rupture and flow in solids. *Philosophical Transactions of the Royal Society of London. Series A*, **221**, 163–198.

[26] Tabor, D. (1977) Surface forces and surface interactions. *Journal of Colloid and Interface Science*, **58**, 2–13.

[27] Derjaguin, B.V., Muller, V.M., Toporov, Y.P. (1978) On the role of molecular forces in contact deformations (critical remarks concerning Dr. Tabor's report). *Journal of Colloid and Interface Science*, **67**, 378–379.

[28] Tabor, D. (1978) On the role of molecular forces in contact deformations (critical remarks concerning Dr. Tabor's report). *Journal of Colloid and Interface Science*, **67**, 380.

[29] Derjaguin, B.V., Muller, V.M., Toporov, Y.P. (1980) On different approaches to the contact mechanics. *Journal of Colloid and Interface Science*, **73**, 293–294.

[30] Hughes, B.D., White, L.R. (1980) Analytic approximations for the elastic contact of rough spheres. *ASME Journal of Applied Mechanics*, **47**, 194–196.

[31] Muller, V.M., Yushchenko, V.S., Derjaguin, B.V. (1980) On the influence of molecular forces on the deformation of an elastic sphere and its sticking to a rigid plane. *Journal of Colloid and Interface Science*, **77**, 91–101.

[32] Maugis, D. (1992) Adhesion of spheres: The JKR-DMT transition using a Dugdale model. *Journal of Colloid and Interface Science*, **150**, 243–269.

[33] Johnson, K.L., Kendall, K., Roberts, A.D. (1971) Surface energy and the contact of elastic solids. *Proceedings of the Royal Society of London. Series A, Mathematical and Physical Sciences*, **324**, 301–313.

[34] Derjaguin, B.V., Muller, V.M., Toporov, Y.P. (1975) Effect of contact deformations on the adhesion of particles. *Journal of Colloid and Interface Science*, **53**, 314–326.

[35] Muller, V.M., Yushchenko, V.S., Derjaguin, B.V. (1983) General theoretical consideration of the influence of surface forces on contact deformations and the reciprocal adhesion of elastic spherical particles. *Journal of Colloid and Interface Science*, **92**, 92–101.

[36] Hughes, B.D., White, L.R. (1980) Implications of elastic deforrnation on the direct measurement of surface forces. *Journal of the Chemical Society, Faraday Transactions I*, **76**, 963–978.

[37] Zhao, Y.-P., Wang, L.S., Yu, T.X. (2003) Mechanics of adhesion in MEMS—A review. *Journal of Adhesion Science and Technology*, **17**, 519–546.

[38] Sneddon, I.N. (1965) The relation between load and penetration in the axisymmetric boussinesq problem for a punch of arbitrary profile. *International Journal of Engineering Sciences*, **3**, 47–57.

[39] Harding, J.W., Sneddon, I.N. (1945) The elastic stress produced by the indentation of the plane surface of a semi-infinite elastic solid by a rigid punch. *Proceedings of the Cambridge Philosophical Society*, **41**, 16–26.

[40] Oliver, W.C., Pharr, G.M. (1992) An improved technique for determining hardness and elastic modulus using load and displacement sensing indentation experiments. *Journal of Materials Research*, **7**, 1564–1583.

[41] Oliver, W.C., Pharr, G.M. (2004) Measurement of hardness and elastic modulus by instrumented indentation: Advances in understanding and refinements to methodology. *Journal of Materials Research*, **19**, 3–20.

[42] Williamson, J.B.P., Greenwood, J.A., Harris, J. (1956) The influence of dust particles on the contact of solids. *Proceedings of the Royal Society of London. Series A*, **237**, 560–573.

[43] Bowden, F.P., Tabor, D. (1964) *The Friction and Lubrication of Solids. Part II*. Oxford University Press, Oxford, UK.

[44] McFarlane, J.S., Tabor, D. (1950) Adhesion of solids and the effect of surface films. *Proceedings of the Royal Society of London. Series A*, **202**, 224–243.

[45] DelRio, F.W., Dunn, M.L., Phinney, L.M., Bourdon, C.J., de Boer, M.P. (2007) Rough surface adhesion in the presence of capillary condensation. *Applied Physics Letters*, **90**, 163104.

[46] Wang, J., Qian, J., Gao, H. (2009) Effects of capillary condensation in adhesion between rough surfaces. *Langmuir*, **25**, 11727–11731.

[47] Bowden, F.P., Tabor, D. (1950) *The Friction and Lubrication of Solids. Part I*. Oxford University Press, Oxford, UK.

[48] Fuller, K.N.G., Tabor, D. (1975) The effect of surface roughness on the adhesion of elastic solids. *Proceedings of the Royal Society of London. Series A*, **345**, 327–342.

[49] Persson, B.N.J. (1998) On the theory of rubber friction. *Surface Science*, **401**, 445–454.

[50] Cyprien, G. (2002) Stickiness: Some fundamentals of adhesion. *Integrative and Comparative Biology*, **42**, 1123–1126.

[51] Krupp, H. (1967) Particle adhesion theory and experiment. *Advances in Colloid and Interface Science*, **1**, 111–239.

[52] Greenwood, J.A., Williamson, J.B.P. (1966) Contact of nominally flat surfaces. *Proceedings of the Royal Society of London. Series A*, **295**, 300–319.

[53] Butt, H.J., Kappl, M. (2010) *Surface and Interfacial Forces*. Wiley-VCH, Weinheim, Germany.

[54] Rabinovich, Y.I., Adler, J.J., Ata, A., Singh, R.K., Moudgil, B.M. (2000) Adhesion between nanoscale rough surfaces I. role of asperity geometry. *Journal of Colloid and Interface Science*, **232**, 10–16.

[55] Hyun, S., Pei, L., Molinari, J.F., Robbins, M.O. (2004) Finite-element analysis of contact between elastic self-affine surfaces. *Physical Review E*, **70**, 026117.

[56] Persson, B.N.J. (2007) Relation between interfacial separation and load: A general theory of contact mechanics. *Physical Review Letters*, **99**, 125502.

[57] Yang, C., Persson, B.N.J. (2008) Molecular dynamics study of contact mechanics: Contact area and interfacial separation from small to full contact. *Physical Review Letters*, **100**, 024303.

[58] Lorenz, B., Persson, B.N.J. (2009) Interfacial separation between elastic solids with randomly rough surfaces: Comparison of experiment with theory. *Journal of Physics: Condensed Matter*, **21**, 015003.

[59] Benz, M., Rosenberg, K.J., Kramer, E.J., Israelachvili, J.N. (2006) The deformation and adhesion of randomly rough and patterned surfaces. *Journal of Physical Chemistry B*, **110**, 11884–11893.

[60] Bhushan, B. (2003) *Springer Handbook of Nanotechnology*. Springer-Verlag, Berlin, Germany.

[61] Landman, U., Luedtke, W.D., Burnham, N.A., Colton, R.J. (1990) Atomistic mechanisms and dynamics of adhesion, nanoindentation, and fracture. *Science*, **248**, 454–461.

[62] Maeda, N., Chen, N., Tirrell, M., Israelachvili, J.N. (2002) Adhesion and friction mechanisms of polymer-on-polymer surfaces. *Science*, **297**, 379–382.

[63] Chen, N., Maeda, N., Tirrell, M., Israelachvili, J. (2005) Adhesion and friction of polymer surfaces: The effect of chain ends. *Macromolecules*, **38**, 3491–3503.

[64] Zeng, H., Maeda, N., Chen, N., Tirrell, M., Israelachvili, J. (2006) Adhesion and friction of polystyrene surfaces around Tg. *Macromolecules*, **39**, 2350–2363.

[65] Atack, D., Tabor, D. (1958) The friction of wood. *Proceedings of the Royal Society of London. Series A*, **246**, 539–555.

[66] Svensson, B.A., Nystrom, S., Gradin, P.A., Hoglund, H. (2009) Frictional testing of wood—Initial studies with a new device. *Tribology International*, **42**, 190–196.

[67] Bowden, F.P., Moore, A.J.W., Tabor, D. (1943) The ploughing and adhesion of sliding metals. *Journal of Applied Physics*, **14**, 80–91.

[68] Sutton, A.P. (1996) Deformation mechanisms, electronic conductance and friction of metallic nanocontacts. *Current Opinion in Solid State and Materials Science*, **1**, 827–833.

[69] Moore, A.J.W. (1948) Deformation of metals in static and in sliding contact. *Proceedings of the Royal Society of London. Series A*, **195**, 231–244.

[70] Hutchinson, E., Rideal, E.K. (1947) Adsorption and lubrication at crystal surfaces part I. on the boundary lubrication of sodium nitrate. *Transactions of the Faraday Society*, **43**, 435–438.

[71] Luthi, R., Meyer, E., Bammerlin, M., Howald, L., Haefke, H., Lehmann, T., et al. (1996) Friction on the atomic scale: An ultrahigh vacuum atomic force microscopy study on ionic crystals. *Journal of Vacuum Science & Technology B*, **14**, 1280–1284.

[72] Bowden, F.P., Hanwell, A.E. (1966) The friction of clean crystal surfaces. *Proceedings of the Royal Society of London. Series A*, **295**, 233–243.

[73] Ruan, J., Bhushan, B. (1994) Atomic-scale and microscale friction studies of graphite and diamond using friction force microscopy. *Journal of Applied Physics*, **76**, 5022–5035.

[74] Savage, R.H. (1948) Graphite lubrication. *Journal of Applied Physics*, **19**, 1–10.

[75] Bowden, F.P., Young, J.E. (1951) Friction of diamond, graphite, and carbon and the influence of surface films. *Proceedings of the Royal Society of London*, **208**, 444–455.

[76] Mate, C.M., McClelland, G.M., Erlandsson, R., Chiang, S. (1987) Atomic-scale friction of a tungsten tip on a graphite surface. *Physical Review Letters*, **59**, 1942–1945.

[77] Grillo, S.E., Field, J.E., van Bouwelen, F.M. (2000) Diamond polishing: The dependency of friction and wear on load and crystal orientation. *Journal of Physics D: Applied Physics*, **33**, 985–990.

[78] Bailey, A.I., Courtney-Pratt, J.S. (1955) The area of real contact and the shear strength of monomolecular layers of a boundary lubricant. *Proceedings of the Royal Society of London. Series A*, **227**, 500–515.

[79] Hu, J., Xiao, X., Ogletree, D.F., Salmeron, M. (1995) Atomic scale friction and wear of mica. *Surface Science*, **327**, 358–370.

[80] Hirano, M., Shinjo, K., Kaneko, R., Murata, Y. (1991) Anisotropy of frictional forces in muscovite mica. *Physical Review Letters*, **67**, 2642–2645.

[81] Bhushan, B., Burton, Z. (2005) Adhesion and friction properties of polymers in microfluidic devices. *Nanotechnology*, **16**, 467–478.

[82] King, R.F., Tabor, D. (1953) The effect of temperature on the mechanical properties and the friction of plastics. *Proceedings of the Physical Society. Section B*, **66**, 728–736.

[83] McLaren, K.G., Tabor, D. (1963) Visco-elastic properties and the friction of solids. *Nature*, **197**, 856–858.

[84] Brewer, N.J., Beake, B.D., Leggett, G.J. (2001) Friction force microscopy of self-assembled monolayers: Influence of adsorbate alkyl chain length, terminal group chemistry, and scan velocity. *Langmuir*, **17**, 1970–1974.

[85] Grosch, K.A. (1963) The relation between the friction and visco-elastic properties of rubber. *Proceedings of the Royal Society of London. Series A*, **274**, 21–39.

[86] Bowden, F.P., Rowe, G.W. (1955) The friction and the mechanical properties of solid krypton. *Proceedings of the Royal Society of London. Series A*, **228**, 1–9.

[87] Evans, D.C.B., Nye, J.F., Cheeseman, K.J. (1976) The kinetic friction of ice. *Proceedings of the Royal Society of London. Series A*, **347**, 493–512.

[88] Krim, J. (2002) Resource letter: FMMLS-1: Friction at macroscopic and microscopic length scales. *American Journal of Physics*, **70**, 890–897.

[89] Tomlinson, G.A. (1929) A molecular theory of friction. *Philosophical Magazine*, **7**, 905–939.

[90] Bowden, F.P., Moore, A.J.W. (1945) Adhesion of lubricated metals. *Nature*, **155**, 451–452.

[91] Spurr, R.T. (1956) The "ploughing" contribution to friction. *British Journal of Applied Physics*, **7**, 260–261.

[92] McFarlane, J.S., Tabor, D. (1950) Relation between friction and adhesion. *Proceedings of the Royal Society of London. Series A*, **202**, 244–253.

[93] Mroz, Z., Stupkiewicz, S. (1998) Constitutive model of adhesive and ploughing friction in metal-forming processes. *International Journal of Mechanical Sciences*, **40**, 281–303.

[94] Venkatachalam, S., Liang, S.Y. (2007) Effects of ploughing forces and friction coefficient in microscale machining. *Journal of Manufacturing Science and Engineering-Transactions of the ASME*, **129**, 274–280.

[95] Lafaye, S., Gauthier, C., Schirrer, R. (2006) The ploughing friction: Analytical model with elastic recovery for a conical tip with a blunted spherical extremity. *Tribology Letters*, **21**, 95–99.

[96] Zhu, P., Hu, Y., Ma, T., Wang, H. (2011) Molecular dynamics study on friction due to ploughing and adhesion in nanometric scratching process. *Tribology Letters*, **41**, 41–46.

[97] Homola, A.M., Israelachvili, J.N., Gee, M.L., McGuiggan, P.M. (1989) Measurements of and relation between the adhesion and friction of two surfaces separated by molecularly thin liquid films. *Journal of Tribology*, **111**, 675–682.

[98] Yoshizawa, H., Chen, Y.-L., Israelachvili, J. (1993) Fundamental mechanisms of interfacial friction. 1. Relation between adhesion and friction. *Journal of Physical Chemistry*, **97**, 4128–4140.

[99] Yoshizawa, H., Israelachvili, J. (1994) Relation between adhesion and friction forces across thin films. *Thin Solid Films*, **246**, 71–76.

[100] Morgan, F., Muskat, M., Reed, D.W. (1941) Studies in lubrication. X. Friction phenomena and the stick-slip process. *Journal of Applied Physics*, **12**, 743–752.

[101] Bristow, J.R. (1942) Mechanism of kinetic friction. *Nature*, **149**, 169–170.

[102] Berman, A.D., Ducker, W.A., Israelachvili, J.N. (1996) Origin and characterization of different stick-slip friction mechanisms. *Langmuir*, **12**, 4559–4563.

[103] Gee, M.L., McGuiggan, P.M., Israelachvili, J.N., Homola, A.M. (1990) Liquid to solidlike transitions of molecularly thin films under shear. *Journal of Chemical Physics*, **93**, 1895–1906.

[104] Yosbizawa, H., Israelachvili, J. (1993) Fundamental mechanisms of interfacial friction. 2. stick-slip friction of spherical and chain molecules. *Journal of Physical Chemistry*, **97**, 11300–11313.

[105] Thompson, P.A., Robbins, M.O. (1990) Origin of stick-slip motion in boundary lubrication. *Science*, **250**, 792–794.

[106] Israelachvili, J.N., McGuiggan, P.M., Homola, A.M. (1988) Dynamic properties of molecularly thin liquid films. *Science*, **240**, 189–191.

[107] Overney, R.M., Takano, H., Fujihira, M., Paulus, W., Ringsdorf, H. (1994) Anisotropy in friction and molecular stick-slip motion. *Physical Review Letters*, **72**, 3546–3549.

[108] Choi, J.S., Kim, J., Byun, I., Lee, D.H., Lee, M.J., Park, B.H., et al. (2011) Friction Anisotropy–Driven domain imaging on exfoliated monolayer graphene. *Science*, **333**, 607–610.

[109] Bentall, R.H., Johnson, K.L. (1967) Slip in the rolling contact of two dissimilar elastic rollers. *International Journal of Mechanical Sciences*, **9**, 389–404.

[110] Eldredge, K.R., Tabor, D. (1955) The mechanism of rolling friction. I. The plastic range. *Proceedings of the Royal Society of London. Series A, Mathematical and Physical Sciences*, **229**, 181–198.

[111] Tabor, D. (1955) The mechanism of rolling friction. II. The elastic range. *Proceedings of the Royal Society of London. Series A, Mathematical and Physical Sciences*, **229**, 198–220.

[112] Reynolds, O. (1886) On the theory of lubrication and its application to Mr. Beauchamp tower's experiments, including an experimental determination of the viscosity of olive oil. *Philosophical Transactions of the Royal Society of London*, **177**, 157–234.

[113] Hardy, W.B., Doubleday, I. (1922) Boundary lubrication. The paraffin series. *Proceedings of the Royal Society of London. Series A*, **100**, 550–574.

[114] Hardy, W.B., Doubleday, I. (1922) Boundary lubrication. The temperature coefficient. *Proceedings of the Royal Society of London. Series A*, **101**, 487–492.

[115] Bhushan, B., Israelachvili, J.N., Landman, U. (1995) Nanotribology: Friction, wear and lubrication at the atomic scale. *Nature*, **374**, 607–616.

[116] Greene, G.W., Banquy, X., Lee, D.W., Lowrey, D.D., Yu, J., Israelachvili, J.N. (2011) Adaptive mechanically controlled lubrication mechanism found in articular joints. *Proceedings of the National Academy of Sciences of the United States of America*, **108**, 5255–5259.

[117] Raviv, U., Glasson, S., Kampf, N., Gohy, J., Jerome, R., Klein, J. (2003) Lubrication by charged polymers. *Nature*, **425**, 163–165.

[118] Benz, M., Chen, N., Israelachvili, J. (2004) Lubrication and wear properties of grafted polyelectrolytes, hyaluronan and hylan, measured in the surface forces apparatus. *Journal of Biomedical Materials Research Part A*, **71A**, 6–15.

[119] Leroy, S., Steinberger, A., Cottin-Bizonne, C., Trunfio-Sfarghiuab, A., Charlaix, E. (2009) Probing biolubrication with a nanoscale flow. *Soft Matter*, **5**, 4997–5002.

[120] Sivan, S., Schroeder, A., Verberne, G., Merkher, Y., Diminsky, D., Priev, A., et al. (2010) Liposomes act as effective biolubricants for friction reduction in human synovial joints. *Langmuir*, **26**, 1107–1116.

[121] Whitehouse, D.J., Archard, J.F. (1970) The properties of random surfaces of significance in their contact. *Proceedings of the Royal Society of London. Series A*, **316**, 97–121.

[122] Adams, G.G., Nosonovsky, M. (2000) Contact modeling—Forces. *Tribology International*, **33**, 431–442.

[123] Onions, R.A., Archard, J.F. (1973) The contact of surfaces having a random structure. *Journal of Physics D: Applied Physics*, **6**, 289–304.

[124] Gupta, P.K., Cook, N.H. (1972) Statistical analysis of mechanical interaction of rough surfaces. *ASME Journal of Lubrication Technology*, **94**, 19–26.

[125] Nayak, R.P. (1971) Random process model of rough surfaces. *ASME Journal of Lubrication Technology*, **93**, 398–407.

[126] Bowden, F.P., Tabor, D. (1939) The area of contact between stationary and between moving surfaces. *Proceedings of the Royal Society of London. Series A*, **169**, 391–413.

[127] Eguchi, M., Shibamiya, T., Yamamoto, T. (2009) Measurement of real contact area and analysis of stick/slip region. *Tribology International*, **42**, 1781–1791.

[128] Eguchi, M., Yamamoto, T. (2005) Shear characteristics of a boundary film for a paper-based wet friction material: Friction and real contact area measurement. *Tribology International*, **38**, 327–335.

[129] Siegbahn, K., Vetenskaps-societeten i Upsala (1967) *ESCA; Atomic, Molecular and Solid State Structure Studied by Means of Electron Spectroscopy*. Almqvist & Wiksells, Uppsala, Sweden.

[130] Ashkin, A. (1970) Acceleration and trapping of particles by radiation pressure. *Physical Review Letters*, **24**, 156–159.

[131] Ashkin, A., Dziedzic, J.M., Yamane, T. (1987) Optical trapping and manipulation of single cells using infrared laser beams. *Nature*, **330**, 769–771.

[132] Chu, S., Bjorkholm, J.E., Ashkin, A., Cable, A. (1986) Experimental observation of optically trapped atoms. *Physical Review Letters*, **57**, 314–317.

[133] Leckband, D., Israelachvili, J. (2001) Intermolecular forces in biology. *Quarterly Reviews of Biophysics*, **34**, 105–267.

[134] Binnig, G., Quate, C.F., Gerber, C. (1986) Atomic force microscope. *Physical Review Letters*, **56**, 930–934.

[135] Butt, H.J., Cappella, B., Kappl, M. (2005) Force measurements with the atomic force microscope: Technique, interpretation and applications. *Surface Science Reports*, **59**, 1–152.

[136] Hutter, J.L., Bechhoefer, J. (1993) Calibration of atomic-force microscope tips. *Review of Scientific Instruments*, **64**, 1868–1873.

[137] Bhushan, B. (2008) *Nanotribology and Nanomechanics*. Springer, Heidelberg, Germany.

[138] Bhushan, B. (2001) *Modern Tribology Handbook*. CRC Press, Boca Raton, FL.

[139] Tabor, D., Winterton, R.H.S. (1969) The direct measurement of normal and retarded van der Waals forces. *Proceedings of the Royal Society of London. Series A, Mathematical and Physical Sciences*, **312**, 435–450.

[140] Israelachvili, J.N., Tabor, D. (1972) Measurement of van der Waals dispersion forces in the range 1.4 to 130 nm. *Nature Physical Science*, **236**, 106.

[141] Israelachvili, J.N., Tabor, D. (1972) The measurement of van der Waals dispersion forces in the range 1.5 to 130 nm. *Proceedings of the Royal Society of London. Series A*, **331**, 19–38.

[142] Israelachvili, J., Min, Y., Akbulut, M., Alig, A., Carver, G., Greene, W., et al. (2010) Recent advances in the surface forces apparatus (SFA) technique. *Reports on Progress in Physics*, **73**, 036601.

[143] Israelachvili, J.N., Adams, G.E. (1978) Measurement of forces between two mica surfaces in aqueous electrolyte solutions in the range 0–100 nm. *Journal of the Chemical Society, Faraday Transactions 1*, **74**, 975–1001.

[144] Israelachvili, J.N., McGuiggan, P.M. (1990) Adhesion and short-range forces between surfaces. Part I: New apparatus for surface force measurements. *Journal of Materials Research*, **5**, 2223–2231.

[145] Israelachvili, J. (1987) Direct measurements of forces between surfaces in liquids at the molecular level. *Proceedings of the National Academy of Sciences of the United States of America*, **84**, 4722–4724.

[146] Israelachvili, J.N., Adams, G.E. (1976) Direct measurement of long range forces between two mica surfaces in aqueous KNO_3 solutions. *Nature*, **262**, 774–776.

[147] Payne, M.C., Teter, M.P., Allan, D.C., Arias, T.A., Joannopoulos, J.D. (1992) Iterative minimization techniques for ab initio total-energy calculations: Molecular dynamics and conjugate gradients. *Reviews of Modern Physics*, **64**, 1045–1097.

[148] van Gunsteren, W.F., Berendsen, H.J.C. (1990) Computer simulation of molecular dynamics: Methodology, applications, and perspectives in chemistry. *Angewandte Chemie International Edition in English*, **29**, 992–1023.

[149] Frenkel, D., Smit, B. (2002) *Understanding Molecular Simulation: From Algorithms to Applications*, 2nd ed. Academic Press, San Diego, CA.

[150] Cheng, S., Luan, B., Robbins, M.O. (2010) Contact and friction of nanoasperities: Effects of adsorbed monolayers. *Physical Review E*, **81**, 016102.

[151] Cheng, S., Robbins, M.O. (2010) Defining contact at the atomic scale. *Tribology Letters*, **39**, 329–348.

[152] Yang, C., Tartaglino, U., Persson, B.N.J. (2006) A multiscale molecular dynamics approach to contact mechanics. *European Physical Journal E*, **19**, 47–58.

[153] Yang, C., Persson, B.N.J. (2008) Contact mechanics: Contact area and interfacial separation from small contact to full contact. *Journal of Physics: Condensed Matter*, **20**, 215214.

[154] He, G., Müser, M.H., Robbins, M.O. (1999) Adsorbed layers and the origin of static friction. *Science*, **284**, 1650–1652.

[155] Smith, E.D., Robbins, M.O., Cieplak, M. (1996) Friction on adsorbed monolayers. *Physical Review E*, **54**, 8252–8260.

[156] Cieplak, M., Smith, E.D., Robbins, M.O. (1994) Molecular origins of friction: The force on adsorbed layers. *Science*, **265**, 1209–1212.

[157] Gao, J., Luedtke, W.D., Gourdon, D., Ruths, M., Israelachvili, J.N., Landman, U. (2004) Frictional forces and Amontons' law: From the molecular to the macroscopic scale. *Journal of Physical Chemistry B*, **108**, 3410–3425.

[158] Luan, B., Robbins, M.O. (2005) The breakdown of continuum models for mechanical contacts. *Nature*, **435**, 929–932.

[159] Thompson, P.A., Grest, G.S., Robbins, M.O. (1992) Phase transitions and universal dynamics in confined films. *Physical Review Letters*, **68**, 3448–3451.